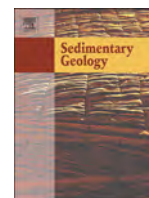


Contents lists available at [ScienceDirect](http://ScienceDirect.com)

Sedimentary Geology

journal homepage: www.elsevier.com/locate/sedgeo

Q1 Controls on space–time distribution of soft-sediment deformation structures: Applying palaeomagnetic dating to approach the *apparent recurrence period* of paleoseisms at the Concud fault (eastern Spain)

Q2 L. Ezquerro ^{a,*}, M. Moretti ^b, C.L. Liesa ^a, A. Luzón ^a, E.L. Pueyo ^c, J.L. Simón ^a

^a Departamento de Ciencias de la Tierra, Universidad de Zaragoza, Pedro Cerbuna 12, 50009 Zaragoza, Spain

^b Dipartimento di Scienze della Terra e Geoambientali, Università degli Studi di Bari, via E. Orabona 4, 70100 Bari, Italy

^c Instituto Geológico y Minero de España, Unidad de Zaragoza, C/Manuel Lasala 44, 50006 Zaragoza, Spain

ARTICLE INFO

Article history:

Received 27 November 2015

Received in revised form 6 June 2016

Accepted 10 June 2016

Available online xxxx

Keywords:

Soft-sediment deformation structure

Seismites

Seismogenic fault

Magnetostatigraphy

Recurrence period

Jiloca Basin

ABSTRACT

This work describes soft-sediment deformation structures (clastic dykes, load structures, diapirs, slumps, 20 nodulizations or mudcracks) identified in three sections (Concud, Ramblillas and Masada Cociero) in the Iberian 21 Range, Spain. These sections were logged from boreholes and outcrops in Upper Pliocene-Lower Pleistocene de- 22 posits of the Teruel-Concud Residual Basin, close to de Concud normal fault. Timing of the succession and hence 23 of seismic and non-seismic SSDs, covering a time span between ~3.6 and ~1.9 Ma, has been constrained from 24 previous biostratigraphic and magnetostratigraphic information, then substantially refined from a new 25 magnetostratigraphic study at Masada Cociero profile. Non-seismic SSDs are relatively well-correlated between 26 sections, while seismic ones are poorly correlated except for several clusters of structures. Between 29 and 35 27 seismic deformed levels have been computed for the overall stratigraphic succession. Factors controlling the lat- 28 eral and vertical distribution of SSDs are their seismic or non-seismic origin, the distance to the seismogenic 29 source (Concud Fault), the sedimentary facies involved in deformation and the observation conditions (borehole 30 core vs. natural outcrop). In the overall stratigraphic section, seismites show an apparent recurrence period of 56 31 to 108 ka. Clustering of seismic SSDs levels within a 91-ka-long interval records a period of high paleoseismic 32 activity with an apparent recurrence time of 4.8 to 6.1 ka, associated with increasing sedimentation rate and 33 fault activity. Such activity pattern of the Concud Fault for the Late Pliocene-Early Pliocene, with alternating 34 periods of faster and slower slip, is similar to that for the most recent Quaternary (last ca. 74 ka BP). Concerning 35 the research methods, time occurrence patterns recognized for peaks of paleoseismic activity from SSDs in 36 boreholes are similar to those inferred from primary evidence in trenches. Consequently, *apparent recurrence* 37 *periods* calculated from SSDs inventories collected in borehole logs close to seismogenic faults are comparable 38 to actual recurrence times of large paleoearthquakes. 39

© 2016 Elsevier B.V. All rights reserved. 40

1. Introduction

The use of soft-sediment deformation structures (SSDs) induced by ground shaking generated by seismic wave (seismites) as a record of past earthquakes is a common practice in sedimentological/stratigraphical (Allen, 1986) and paleoseismological studies (Obermeier, 1996), particularly in ancient to present-day fluvial-lacustrine successions (e.g. Sims, 1975; Davenport and Ringrose, 1987, 1975; Guiraud and Plaziat, 1993; Van Loon et al., 1995; Alfaro et al., 1997; Rodríguez-Pascua et al., 2000; Migowski et al., 2004; Moretti and Sabato, 2007; Moretti and Ronchi, 2011; Stárková et al., 2015). After the innovative work by Sims (1975), many authors have tried to evaluate the recurrence time

of past earthquakes by analyzing the vertical repetition of deformed beds in lacustrine successions. Nevertheless, this approach involves some limitations (Montenat et al., 2007; Owen et al., 2011; Moretti and van Loon, 2014) related with the fact that some earthquakes may not be recorded in the sedimentary succession (Moretti et al., 1999) or that a single seismic shock can induce superimposed deformed beds (Gibert et al., 2011).

Recently, after recognizing 21 seismite levels in a 75-m-long borehole through Upper Pliocene-Lower Pleistocene lacustrine deposits of the Teruel Basin (Masada Cociero site), Ezquerro et al. (2015) have proposed the concept of *apparent recurrence period*, as the inverse of the frequency of occurrence of seismites per unit time along a borehole. The term 'apparent' refers to the fact that the paleoseismic record at a given point is a partial one, since the spatial distribution of SSDs produced by an individual event (and so its probability of being

* Corresponding author. Tel.: +34 976 76 10 81; fax: +34 976 86 11 06.
E-mail address: lope@unizar.es (L. Ezquerro).

represented at a given site) is limited. In this way, after accepting that subsidence and sedimentation rates were fairly similar, Ezquerro et al. (2015) have estimated an apparent recurrence period of about 45–51 ka for the Masada Cociero borehole log. They also discussed the quality and representativeness of observations of SSDs in well cores by comparing them with those in natural outcrops. The latter have the advantage of lateral continuity, hence the feasibility for recognizing large-scale SSDs, whereas well cores, virtually continuous along the entire sedimentary succession, allow detailed observations of fresh rock at a millimeter scale. Reconstructing the paleoseismic record of an area can benefit from combining both data sources, especially if that information from multiple wells is available, allowing correlation of deformed levels in the subsoil. This work goes deeper into this issue, revisiting the same area within the central Teruel Basin (Fig. 1), collecting new surface and subsoil data, and combining multiple research lines in order to reconstruct both the lateral and vertical distribution of SSDs.

First, a new borehole drilled at Ramblillas site, west of Masada Cociero, together with a new surface profile surveyed close to Conclud village (see location in Fig. 2), have enlarged our SSDs record in the Upper Pliocene–Lower Pleistocene succession. Since the Masada Cociero section also combines a well log and a surface profile, the final available SSDs inventory adequately combines both data sources.

Second, we have improved the temporal framework of the paleoseismic occurrences. The age of the Masada Cociero succession was constrained by (i) overall correlation with regional lithostratigraphical units, biostratigraphically by numerous mammal sites and a few magnetostratigraphic profiles (one of them at the Conclud section; Opdyke et al., 1997), and (ii) a mammal site (*Rotonda Teruel-Centro, RTC*; MN 17 zone) located at the Masada Cociero surface profile, which dates these materials to the middle Villafranchian (Ezquerro et al., 2012b). We now add a new magnetostratigraphic study of the Masada Cociero well log, which refines the chronostratigraphy of the studied deposits and provides a more robust correlation of the three surveyed sections. This allows the lateral continuity of deformation structures associated to each paleoseismic event to be assessed, as well as obtaining their precise time distribution along

the surveyed profiles, and thus a better calculation of the apparent recurrence period.

The central Teruel Basin is a perfect target for this kind of study since: i) the instrumental and historical seismicity are well-known; ii) the Late Pliocene–Early Pleistocene is recorded by a thick, continuous alluvial-palustrine-lacustrine succession, suitable for dating by magnetostratigraphic methods; and iii) the structure and paleoseismicity of the most active fault in the area, the Conclud Fault, are well known (Moissenet, 1983; Simón, 1983; Gutiérrez et al., 2008; Lafuente, 2011; Lafuente et al., 2011a, 2014; Simón et al., 2012, 2015; Ezquerro et al., 2014b).

Our objectives are: (i) to describe the SSDs that occur at various stratigraphic levels in the Conclud–Teruel area, both in outcrops and well logs; (ii) to distinguish seismically from non-seismically induced SSDs; (iii) to establish the time distribution of SSDs in different stratigraphic sections, achieving reliable correlations between deformed beds; and iv) to calculate the *apparent recurrence period* of paleoseismic events and discuss the significance of the results.

2. Geological setting

The study area extends along a section transverse to the Conclud Fault, which is located at the junction of the Teruel and Jiloca grabens, in the NE of the Iberian Peninsula (Fig. 1a). These basins represent the most landward structures developed within the Iberian Plate in relation to Neogene rifting at the Valencia Trough, Mediterranean Sea (Álvarez et al., 1979; Simón, 1983; Capote et al., 2002). They evolved through two distinct rift episodes (Simón, 1982, 1983): the first one gave rise to the Teruel Graben (NNE–SSW trend) during the Late Miocene, and the second produced the NNW–SSE trending Jiloca Graben and reactivated the Teruel Graben in the Late Pliocene–Quaternary (Capote et al., 2002).

The northern sector of the Teruel Basin is a half graben with an active eastern boundary formed by a NNW–SSE and NNE–SSW trending fault system (Fig. 1b). The basin fill comprises Upper Miocene to Lower Pleistocene deposits whose age is well constrained by abundant mammal sites and magnetostratigraphic profiles (e.g. Adrover et al., 1978; 149

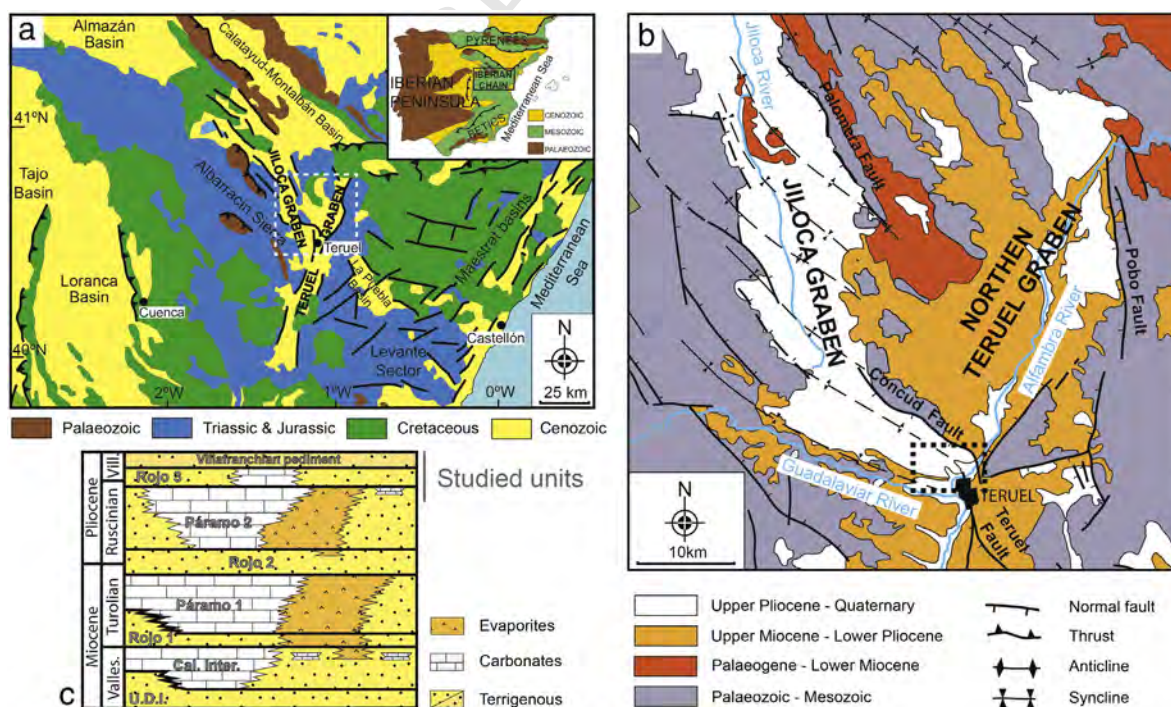


Fig. 1. (a) Neogene–Quaternary extensional basins and the main active faults in the central–eastern Iberian Chain. Inset: location of the study area within the Iberian Peninsula. (b) Geological map of the Jiloca and Teruel basins, with location of the studied area. (c) Stratigraphic units by Godoy et al. (1983a, 1983b).

Adover, 1986; Mein et al., 1983, 1990; Alcalá et al., 2000; Krijgsman et al., 1996; Opdyke et al., 1997; Garcés et al., 1999; van Dam et al., 2001; van Dam, 2006). The succession comprises endorheic red clastic alluvial deposits ~500 m-thick that grade laterally into lacustrine carbonate and gypsum deposits (Weerd, 1976; Godoy et al., 1983a, 1983b; Moissenet, 1980; Alcalá et al., 2000; Alonso-Zarza and Calvo, 2000; Alonso-Zarza et al., 2012; Ezquerro et al., 2012a, 2014a) divided the basin infill into eight lithological units (Fig. 1c) based on the alternation of carbonate (*Calizas Inferiores*, *Páramo 1* and *Páramo 2*) and terrigenous (*Unidad Detrítica Inferior*, *Rojo 1*, *Rojo 2* and *Rojo 3*) units; this succession culminates with a thin alluvial unit (*Villafranchian pediment*). These units have traditionally been used in national geological maps and represent the initial temporal framework for our purposes.

The asymmetric Jiloca Graben is limited in the East by a NNW–SSE *en-echelon* normal fault system (from north to south: Calamocha, Palomera and Concud faults), the Concud Fault being the southernmost structure (Fig. 1b). The infill features are less well known than in the Teruel Basin as only a 70 m-thick succession crops out located towards the South. Several boreholes in the area indicate that the infill reaches up to 130 m northwards (Rubio and Simón, 2007). The age of the uppermost deposits infilling the endorheic basin prior to the incision of the present-day fluvial network, is well constrained to the Late Pliocene–Early Pleistocene from several mammal sites and magnetostratigraphic profiles (e.g. Mein et al., 1983, 1990; Opdyke et al., 1997; van Dam, 2006; Ezquerro et al., 2012b, 2015). The scarce outcrops in combination with subsurface data indicate that interbedded alluvial fan and palustrine deposits filled the basin, equivalent to the *Páramo 2*, *Rojo 3* and *Villafranchian pediment* units defined in the Teruel Basin (Moissenet, 1982; Rubio and Simón, 2007; Ezquerro et al., 2012b, 2015).

The linkage of the Teruel and Jiloca grabens occurred during the Late Pliocene (~3.6 Ma), when the Concud Fault developed (Simón, 1983). The fault has a length of ca. 14.2 km, dip 65° to 70°W, and a general NW–SE strike, which veers to NNW–SSE towards the southern tip, where the Jiloca Graben articulates with the Teruel Graben. Sedimentation was interrupted in the footwall (Teruel Basin) at the end of deposition of the *Páramo 2* unit (Godoy et al., 1983a, 1983b) when the depocentre migrated to the north, towards the Pobo Fault. In the hanging-wall block (Jiloca Basin), lacustrine–palustrine sedimentation was restricted to a small subsiding area close to the Concud Fault surface, the Concud–Teruel Residual Basin (e.g. Moissenet, 1982; Lafuente et al., 2011b; Ezquerro et al., 2012b, 2015). These deposits connected upstream with the distal sectors of alluvial fans fed from the west (Ezquerro et al., 2012b). These sediments correspond to the *Rojo 3* + *Villafranchian Pediment* units (Godoy et al., 1983a, 1983b). During the Early Pleistocene, the hydrological regime changed in both basins to exorheic conditions (Ezquerro et al., 2012b). The Miocene–Pliocene deposits were dissected whereas short alluvial fans and three fluvial terrace levels developed (Godoy et al., 1983a, 1983b; Peña et al., 1984).

The Concud Fault is the main active structure in the area, and the boreholes and outcrops surveyed for this work are located very close (0.2 to 2.0 km) to its trace (Fig. 2a); therefore, it should be considered as the main source for the paleoseisms interpreted from SSDSs. Recent paleoseismological studies of Quaternary deposits affected by the Concud Fault have recognized eleven events between ca. 74 ka BP and the present day (e.g., Lafuente, 2011; Lafuente et al., 2011b, 2014; Simón et al., 2015). The average recurrence period has been calculated as between 7.1 ± 3.5 and 8.0 ± 3.3 ka, with a total net accumulated slip of about 20.5 m and an average coseismic slip of 1.9 m. The displacement pattern shows alternating periods of faster slip (up to 0.53 mm/a) and slower slip (0.13 mm/a), resulting in an average slip rate of 0.29 mm/a. The characteristic earthquake at the Concud Fault is estimated at $M_w = 6.5$ – 6.6 (Ezquerro et al., 2015; Simón et al., 2015).

The Teruel Fault is a second potential seismogenic source in the area; it exhibits a 9 km-long trace, and its characteristic earthquake is estimated at $M_w = 6.1$ – 6.6 (Simón et al., in press). Our studied sites are located at distances of 1.8 to 4.4 from this fault. This structure was

initiated ~3.6 Ma ago, as a blind fault south of Teruel city, then propagated upwards and northwards up to acquiring its present-day trace. A hypothetical propagation towards the study area could occur after Middle Pleistocene time (Lafuente et al., 2011b; Simón et al., in press). Therefore, for the studied succession and time interval (Late Pliocene–Early Pleistocene), the Teruel Fault was smaller and farther than the Concud Fault, so it could only represent a minor seismic source.

3. Sedimentary succession of the Concud–Teruel Residual Basin

The characterization of the sedimentary succession of the Late Pliocene Concud–Teruel Residual Basin is mainly derived from three detailed stratigraphic sections studied in the field (Masada Cociero, Ramblillas and Concud sections), as well as a log of continuous cores recovered in two wells (Masada Cociero and Ramblillas). Combination of surface and subsurface information has allowed the construction of three complete stratigraphic profiles from different sectors of the basin, as well as a facies associations map (Fig. 2). In the eastern sector, the basin infill consists of a syn-tectonic palustrine–lacustrine succession, comprising silty carbonates, marls, limestones and coal beds, that progressively passes towards the west into alluvial deposits comprising mudstones, sandstones and conglomerates (see Ezquerro et al., 2012b, 2015).

The Masada Cociero profile (1 in Fig. 2) was described in detail by Ezquerro et al. (2012b, 2015). It is a composite profile located close to the Concud Fault that comprises a 13.7 m-thick outcropping succession and a 75 m-thick subsurface succession drilled at the bottom of the outcrop. A gap of 12 m due to the Alfambra River incision and Quaternary sedimentation interrupts continuity between both. The lower part of the succession consists of whitish carbonate and evaporite deposits that grade up into reddish mudstones and darkish silts; the succession is more terrigenous towards the top, with mudstones and occasional intercalations of brown sandstones and red conglomerates, but a carbonate-dominated part can be recognized towards the middle of the profile. The RTC mammal site (MN 17 zone), Middle Villafranchian in age (Ezquerro et al., 2012b), is situated at the base of the outcropping series (see Fig. 2). These sediments mainly correspond to the *Rojo 3* unit of Godoy et al. (1983a, 1983b), although the whitish carbonate and evaporite deposits at the base of the well log could correspond to the pre-tectonic *Páramo 2* unit. A new magnetostratigraphic profile has been made to constrain the age of this succession (see below).

As in the previous case, the 45.6 m-thick Ramblillas composite profile (2 in Fig. 2) includes a 5.4 m-thick outcropping succession and a 40.2 m-thick subsurface succession drilled at the bottom of the outcrop. The basal deposits are pale-colored carbonate silts, darkish marls and red mudstones. Above them, the succession is dominantly clastic (orange mudstones and sandstones), but some interbedded carbonate (darkish marls and whitish silts) and brown conglomerate beds also appear. The profile corresponds to the *Rojo 3* unit of Godoy et al. (1983a, 1983b) except for the upper part of the section, where a tabular body of grayish conglomerates has been ascribed to the *Villafranchian pediment* unit (Ezquerro et al., 2012b). This distinctive body has also allowed the physical correlation with the Concud profile (Fig. 3). According to regional data, its age can be attributed to the Late Pliocene (~3.0–2.1 Ma).

The Concud profile (3 in Fig. 2) was entirely logged from outcropping materials and comprises a 49.8 m-thick succession conformably lying on the whitish limestones and marl of the *Páramo 2* unit (Godoy et al., 1983a, 1983b). Its lower part (0 to 24 m) is very heterogeneous, with carbonate deposits, mainly tabular beds of darkish marls, whitish silts, and grayish limestones, orange mudstones and sandstones. The upper part (25 to 50 m) is more clastic, being made up of orange mudstone and sandstone tabular strata with scarce marl intercalations. The top of the section consists of grayish conglomerate bodies (tabular or channeled) with intercalated mudstone beds, which have been attributed to the *Villafranchian pediment* unit. The presence

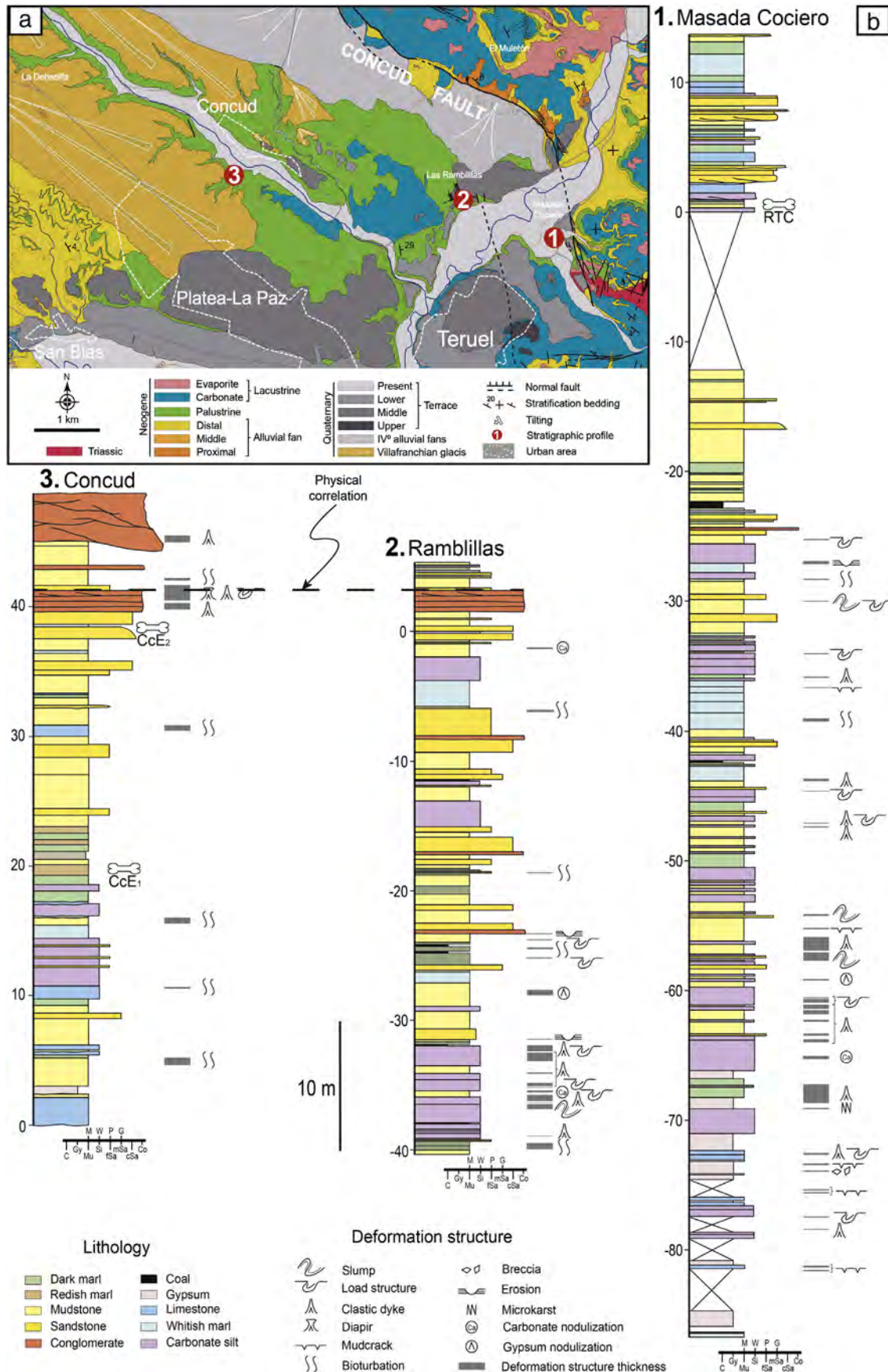


Fig. 2. Stratigraphic profiles along the Concud-Teruel Residual Basin (2 km north of Teruel), see location in Fig. 2a. The Ramblillas and Masada Cociero profiles correspond with composite sections, borehole data and surface data are displaying in negative and positive numbers, respectively.

280 of the *Concud Estación* mammal site (MN 16 zone) of Early Villafranchian
281 age (Mein et al., 1990) and the Concud magnetostratigraphic profile
282 (Opdyke et al., 1997) allow the age of this profile to be bracketed between
283 3.0 and 2.1 Ma.

284 4. Paleomagnetic study of the Masada Cociero profile

285 Magnetostratigraphy is a good method for dating sedimentary
286 sequences (Opdyke and Channell, 1996). The reconstruction of a
287 reliable local polarity sequence (LPS) allows comparison to the Global
288 Polarity Time Scale (GPTS) and dating of polarity boundaries found in
289 that sequence. This brackets the resolution of the method but still per-
290 mits the identification of a number of isochrones in the stratigraphic re-
291 cord. Previous studies in the basin (Krijgsman, 1996; Krijgsman et al.,
292 1996; Opdyke et al., 1997; Sinusia et al., 2004) make us confident
293 about the suitability of this technique to provide a temporal constraint
294 in our study.

295 The paleomagnetic study was performed in the Masada Cociero suc-
296 cession, aiming to find as many magnetozones as possible, searching for
297 an independent calibration to the GPTS and thus, the dating of the stud-
298 ied section. This profile was selected due to: i) the availability of the RTC
299 mammal site (MN17 zone) to help in the correlation with the Concud
300 magnetostratigraphic profile (Opdyke et al., 1997); ii) the occurrence
301 of a large number of SSDSs; and iii) the possibility of establishing a tem-
302 poral model for the distribution of SSDSs to clarify their environmental
303 significance. In this section, only the main results concerning the paleo-
304 magnetic components, the establishment of the Local Polarity Sequence
305 (LPS), and its correlation to the Global Polarity Time Scale (GPTS) will be
306 discussed. Sampling and laboratory procedures, rock magnetism de-
307 magnetization results and details on the Characteristic Remanent Mag-
308 netizations (ChRM) are included in Appendix A.

309 4.1. Paleomagnetic components

310 The intensity of the Natural Remanent Magnetization (NRM)
311 spreads from weak values ($< 100 \cdot 10^{-6}$ A/m) to relatively high ones
312 ($30,000 \cdot 10^{-6}$ A/m), although ~76% of the distribution displays intensi-
313 ties above 1 mA/m and 18% below 0,1 mA/m (Fig. 3). The demagnetiza-
314 tion of the NRM shows the occurrence of relatively simple and noisy
315 paths. The paleomagnetic signal is slightly scattered, which is related
316 to the diversity of rock types and their variable magnetic stability. A re-
317 markable difference in NRM intensities is observed, up to three orders of
318 magnitude higher in reddish mudstones, marls and sandstones than in
319 limestones, carbonate silts and gypsums (Fig. 3). The Isothermal Remanent
320 Magnetization (IRM) acquisition curves outline the contribution of
321 different magnetic minerals to the remanence. The remanence in Masa-
322 da Cociero is mainly carried by magnetite, although iron sulfides and he-
323 matite also contribute in some cases (Appendix A).

324 A secondary low-temperature Viscous Remanent Magnetization
325 (VRM) has been observed in most samples. The VRM component is
326 unblocked in the 20–200 °C interval, but in some samples it can be
327 tracked up to 300–350 °C and contributes to the noisy pattern observed.
328 Apart from a viscous component, 43% of samples showed intermediate
329 unblocking temperatures up to 550 °C. Finally, a high temperature com-
330 ponent is dominant (57% of samples) and can be tracked up to 660–
331 680 °C. The Characteristic Remanent Magnetization (ChRM) has been
332 always defined in these last two unblocking intervals and, as a general
333 rule, normal and reverse polarity samples tend to address the coordi-
334 nate origin in the orthogonal diagrams (Appendix A).

335 The secondary low-temperature VRM component is assumed to re-
336 cord the present-day field and is therefore a potential tool for orienting
337 the samples recovered from the rotation-drilling core (Fuller, 1969;
338 Bleakly et al., 1985; Stokking et al., 1993; Thibal et al., 1999; Zhang
339 et al., 2007). This assumption is confirmed by analyzing oriented
340 samples collected from outcropping rocks at the upper part of the
341 profile: the VRM direction (declination 033° , inclination 56° ; α_{95} :

14.7°, k: 3.2 and R: 0.7022) is not far from the present-day geomagnetic
342 field (355° , 56°) deduced from the NOAA's National Geophysical Data
343 Center using the IGRF12-gufm1 model (Jackson et al., 2000). Accord-
344 ingly, the samples from the well core were oriented using the VRM
345 direction (thermal interval) to the present-axial-dipole field (Fuller,
346 1969; Van der Voo and Watts, 1978; Shibuya et al., 1991; Hailwood
347 and Ding, 1995). The only disadvantage of this method is the transfer-
348 ence of the fisherian noise of the VRM to the ChRM direction. The
349 pseudoantipodality found between the normal and reverse means in
350 our dataset after the correction validates the re-orientation methodol-
351 ogy used in this work (Appendix A), although steepening of the vectors
352 induced by the coring of the well cannot be ruled out. 353

4.2. Local polarity sequence (LPS)

354 The absence of original orientations prevents us applying more
355 rigorous filtering methods (Deenen et al., 2011) to build a sound
356 and reliable LPS. Therefore, we have classified the ChRM directions
357 into three groups to avoid unnecessary noise in the LPS: class I samples
358 (30% of samples) are reliable directions addressed to the origin; class II
359 samples (40%) are poorer quality directions but polarity is unambigu-
360 ous; class III (30%) includes the remaining (low-quality) set of samples,
361 which were not used in any further processing of the data (Appendix A).
362 The Masada Cociero LPS is based on 180 reliable samples, which repre-
363 sent about 60% of successful demagnetizations (Fig. 4). The consistency
364 of the constructed LPS is also founded on the magnetozone pattern: as
365 will be shown later, ChRM from classes I and II were used to calculate
366 the paleo-latitude of the Virtual Geomagnetic Pole (VGP). Despite
367 the slightly noisy signal and the moderate quality of the magnetization,
368 all these criteria help to build a consistent and reliable LPS in which 8
369 different magnetozones were recognized (Fig. 4). 370

371 The profile starts with a reversed zone (R1), which spreads along
372 9 m with 3 levels of class I. Despite the small number of levels with re-
373 liable polarity, almost 20 reversed polarity levels of low quality also fall
374 this magnetozone. N1 starts just above, and covers 8.5 m (5 consecutive
375 levels). R2 is developed between -70 to -68 m (two class I levels). N2
376 spans along the next 16.4 m. R3 occurs from -51.6 to -49.5 m and is
377 defined by one class I level together to several levels of class II. N3 rep-
378 resents 20.5 m; despite the density of samples in this portion of the pro-
379 file, some noise prevents a clearer definition of this zone, although the
380 dominance of the normal polarity cannot be questioned. In the R4
381 local zone (from -28 to 7.4 m) the reverse dominant polarity is punc-
382 tually obscured by a few normal samples. Unfortunately, the middle
383 part of R4 is not represented; as explained in Section 3, it is substituted
384 in the upper part of the Masada Cociero well core by a 12 m-thick suc-
385 cession of clastic fluvial facies, corresponding to a Pleistocene fluvial ter-
386 race incised in Pliocene sediments (Ezquerro et al., 2015). The strong
387 inconsistency with the LPS is corroborated by the highly grouped decli-
388 nations and normal polarity close to 50° of inclination obtained for sam-
389 ples from such upper sediments (likely Bruhnes magnetic period). Right
390 on top of R4, the uppermost magnetozone (N4) can be more clearly de-
391 lined with 6.3 m (4 levels) of normal polarity just below the end of
392 the profile. N3 and R4 represent the noisiest portion of the Masada
393 Cociero LPS. 393

4.3. Correlation of the Masada Cociero LPS to the GPTS

394 Once the Masada Cociero LPS has been built, its integration with the
395 biostratigraphic assignment of the RTC mammal site and other addition-
396 al constraints help to propose a reasonable correlation with the GPTS
397 (Ogg, 2012). Following Ezquerro et al. (2012b), the mammal fauna asso-
398 ciation at the RTC site (e.g. *gazella borbonica*, *Stephanorhinus etruscus*
399 and *Equus stenonis*) is characteristic of mammal zone MN17 (Mein,
400 1975). Thus, the presence of *Equus stenonis* determines a Villafranchian
401 age, which is similar to that ascribed for the neighboring (see location in
402 Fig. 1a) classic mammal site of *La Puebla de Valverde* (MN17, Adrover
403 Q9

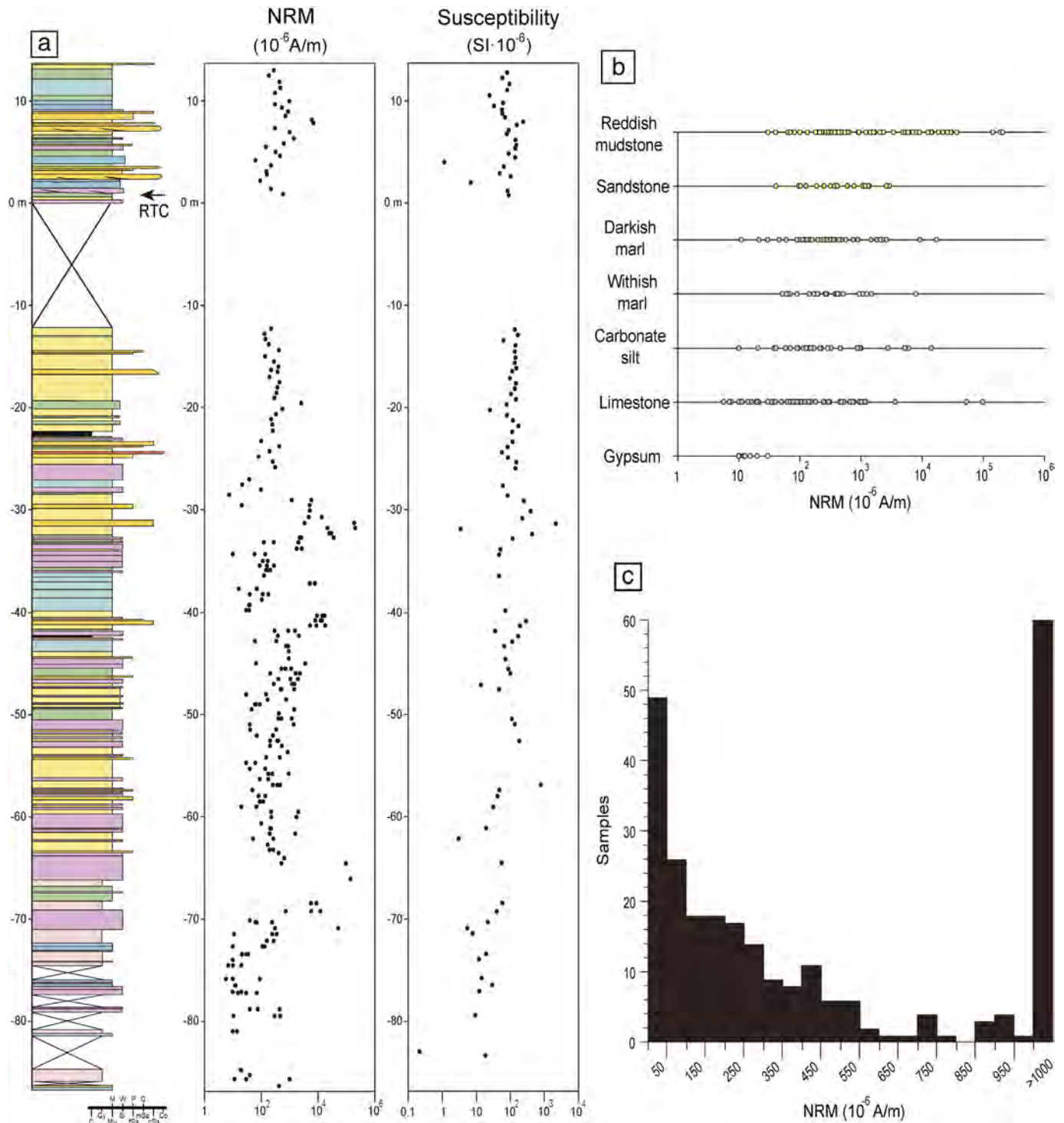


Fig. 3. Magnetic parameters. Natural remanent magnetization and bulk susceptibility in the Masada Cociero section. NRM has been also plotted against lithology (upper right) and a histogram of NRM and k are also shown (lower right).

et al., 1978), which was analyzed by magnetostratigraphy and correlated with chron C2r.1r (middle Villafranchian, Sinusía et al., 2004). In addition, from mammal site information (e.g. Concul Estación site, Mein et al., 1990) and magnetostratigraphic profiling (e.g. Concul profile, Opdyke et al., 1997), our targeted Rojo 3 and Villafranchian pediment units can be dated as Upper Pliocene–Lower Pleistocene. The reader is referred to Fig. 9 by Ezquerro et al. (2012b), in which a compilation of the correlation and ages of these units along the Teruel and Jiloca basins is displayed.

This bio- and magnetostratigraphic frame brackets the time interval represented by the Masada Cociero LPS between the latest Ruscinian and the end of the Villafranchian (Fig. 5). The long reversed portion at the top of the profile (R4) must necessarily belong to the C2r chron (Matuyama), and thus the relation between N4 and C2n seems clear, i.e. the Olduvai subchron. In this way, R4 would correspond to the base of the Matuyama reversed chron. Following this reasoning, N3 + R3 have been correlated with C2An.1 (top of C2An) within the Gauss chron, and N2 + R2 correspond to C2An.2 (middle of C2An).

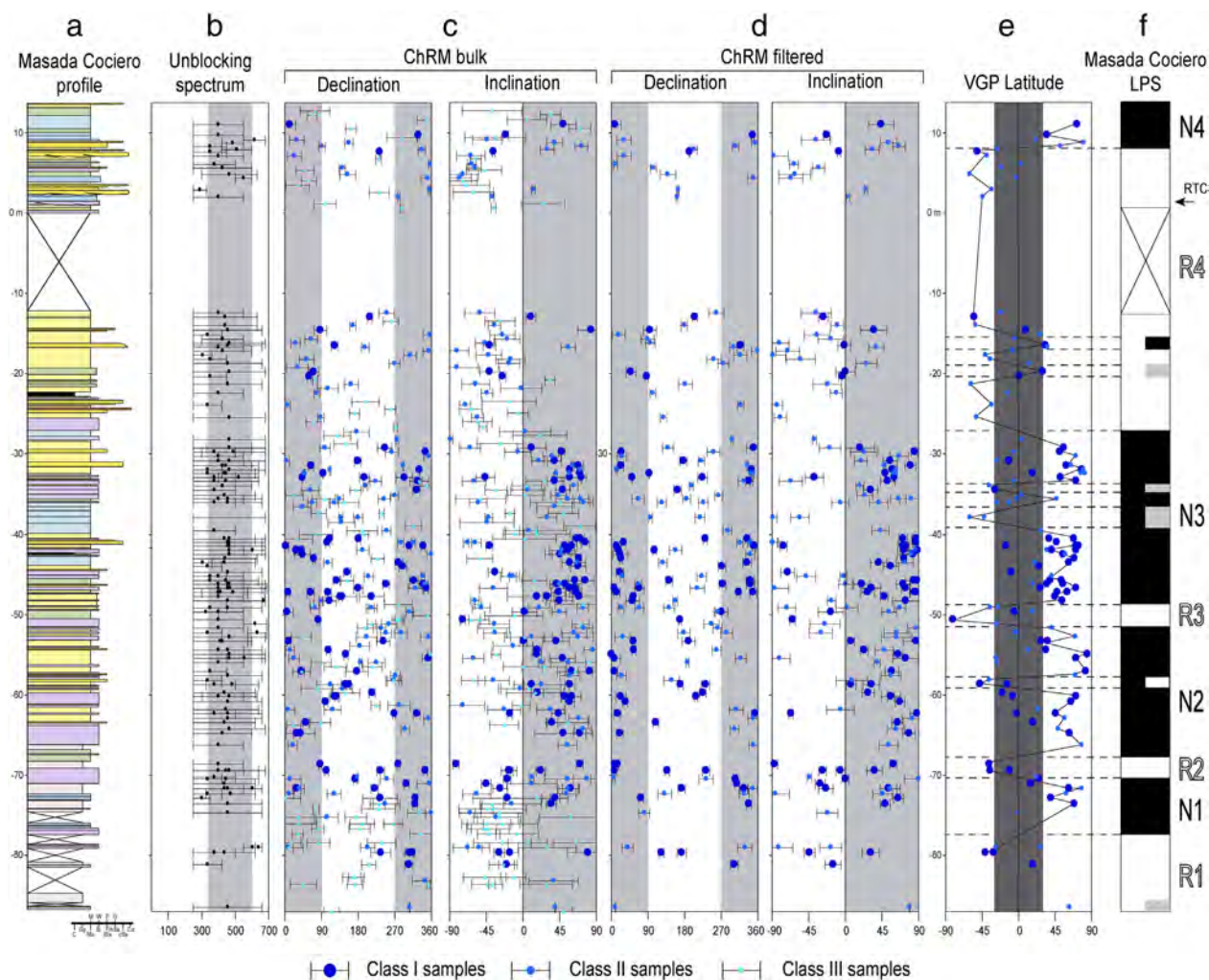


Fig. 4. Magnetostratigraphy in the Masada Cociero composite section; paleomagnetic logs. (a) Lithology. (b) Unblocking spectrum. (c) Declination and inclination of the ChRM of the total samples. (d) Declination and inclination of the ChRM of the total samples. (e) Latitude of the VGP. (f) Local polarity sequence (LPS). Error bars represent the α_{95} confidence angle. The size of the points refers to the quality of data.

422 Thus, R3 would be Kaena subchron and, tentatively, R2 the Mammoth
 423 one. This later correlation is supported by the longer length and better
 424 quality found in R2 against the small reversed interval found between
 425 R2 and R3. We believe N3 could correspond to the top of the Gauss nor-
 426 mal chron (C2An). Then, the long R1 local zone could be assigned to the
 427 top of the long-lasting C2Ar chron (Gilbert reversed chron). According
 428 to our interpretation, the base of the Masada Cociero section (R1/N1
 429 boundary) could fit to the C2Ar/C2An, limit located around the
 430 Ruscinian-Villafranchian boundary. On the other hand, the unstable
 431 normal polarity samples found at the base of R4 could correspond to
 432 the Reunion subchron, although the reliability of this local zone is
 433 uncertain.

434 5. Stratigraphic correlation and age of the involved sediments

435 Stratigraphic correlation of the studied profiles has been mainly
 436 based on physical correlation of beds, vertical trend of sedimentary
 437 facies, and magnetostratigraphic data (both published and new). The lat-
 438 ter have allowed chronological refinement of the studied sediments.
 439 Since most of the studied sediments do not crop out, physical correla-
 440 tion of beds was only possible for a tabular conglomerate package locat-
 441 ed at the upper part of the Conclud and Ramblillas profiles (Fig. 6). This
 442 1.5 m-thick tabular deposit has been physically correlated from visual
 443 inspection during fieldwork, as well as from analysis of 1:18,000-scale
 444 aerial photographs and 1:5000-scale satellite orthoimages.

The vertical trend of sedimentary facies has been used as a powerful 445
 tool in the correlation of stratigraphic sequences, especially for 446
 siliciclastic units (Posamentier and Allen, 1999). In our case, the 447
 construction of the vertical evolution curve has been made using the 448
 following procedure: 449

- i) Lithological types were grouped according to their environmen- 450
 tal significance, assigning a numerical value that refers to their 451
 relative proximal/distal position: alluvial (value 5), mudflat 452
 (value 4), palustrine (value 3), shallow lacustrine (value 2) and 453
 lacustrine (value 1). 454
- ii) Arithmetic means of such values were calculated for each meter 455
 of the stratigraphic succession (values were weighted according 456
 to the thickness of each lithological group). 457
- iii) These mean values were smoothed by applying a 3-point moving 458
 average. 459

The curves so obtained, reflecting some alternating episodes of allu- 461
 vial progradation and lacustrine expansion, has been plotted along the 462
 corresponding stratigraphic profiles in Fig. 6. Comparison between pro- 463
 files has allowed the recognition of similar trends between them, which 464
 have enabled the correlation of the three successions. Below chron 465
 C2r.2r, the proposed correlation is based on the vertical trend curves, 466
 so that the maxima (and minima) of the trend curve located in a similar 467

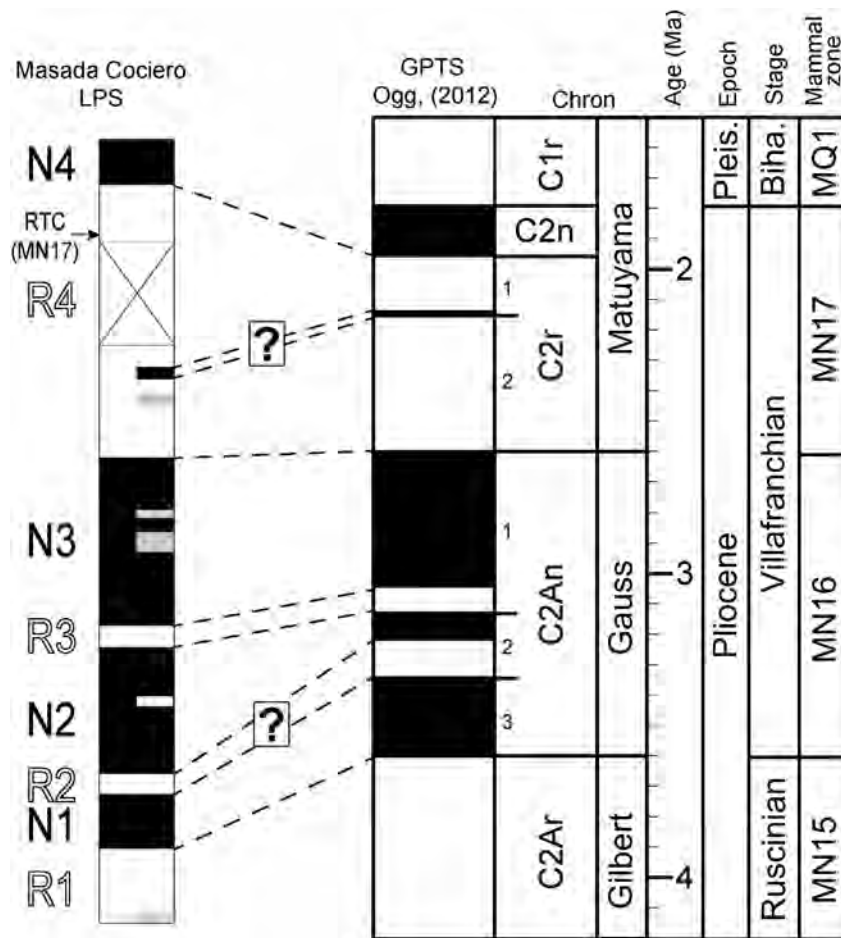


Fig. 5. Correlation of the Masada Cociero LPS with the Global Polarity Time Scale (GPTS) (Ogg, 2012).

stratigraphical position of each succession are considered isochronous. Accordingly, in addition to the basal, pre-tectonic *Páramo 2* unit of the easternmost section, eight sub-units (I to VIII) have been distinguished within the *Rojo 3* unit and the overlying *Villafranchian pediment* unit. Such subunits are not based on simple lithological criteria, but in the vertical trend curve, with each subunit comprising the materials between two consecutive lower values. Overall, the Concud (western) section displays higher absolute values than the Masada Cociero (eastern) section, reflecting the proximal-distal polarity of the sedimentary system.

The magnetostratigraphic results obtained in the Masada Cociero section have allowed us to constrain the age of the sediments. The previously distinguished sub-units range in age between ~3.6 and ~1.8 Ma (Fig. 6). Magnetostratigraphy proposed for the Concud profile by Opdyke et al. (1997), who located the C2An.1–C2r.2 boundary at the upper part of the section (Fig. 6), provides additional constraints and is in accordance with our results in Masada Cociero section. Our study provides greater precision than that conducted by Opdyke et al. (1997), which was carried out with a variable and wider (>5 m) sampling interval. The above-mentioned boundary is now located ca. 3 m lower than the original proposal by Opdyke et al. (1997). The strong constraint of this boundary in our W-E cross-section is the basis for using it as the datum for stratigraphic correlation.

On the other hand, if the thickness of chrons and subchrons recorded in the Masada Cociero LPS is compared with the GPTS, sedimentation rates for the whole studied succession and for each chron and subchron can be displayed and calculated (Fig. 7). The average sedimentation rate for the succession is ca. 0.06 mm/a, i.e. slightly lower than the maximum

rate (0.07 to 0.08 mm/a) previously estimated from the total displacement of the top of *Páramo 2* unit (Ezquerro et al., 2015). However, two episodes of, first, lower (0.02 mm/a) and, then, higher (0.13–0.17 mm/a) sedimentation rate affect the lower part of the C2An chron and the whole C2r chron, respectively.

6. Soft-sediment deformation structures

Soft-sediment deformation structures (SSDs) occur at many stratigraphic levels in the three studied sections, located up to 5 km from the Concud Fault. Detailed descriptions of the SSDs in the Masada Cociero well core were provided by Ezquerro et al. (2015). More than 35 deformed beds (21 interpreted as seismically-induced) were investigated, allowing the reliability of palaeoseismic studies from the well cores to be assessed. We refer to the work by Ezquerro et al. (2015) for descriptions of deformed beds and interpretations of deformation mechanisms and triggers.

In the present work we describe SSDs from the Ramblillas well core (similar to those described in the Masada Cociero well core) and from the Concud outcrops. A total of 28 deformed levels have been observed, 20 in the Ramblillas well core and 8 in the Concud section (Fig. 6). The well core has been studied at a millimeter-scale (Figs. 8, 10), whereas in the Concud outcrops centimetric to metric-scale observations were usually made (Fig. 9). Next, we focused on describing SSDs produced by liquidization and fluidization processes, discarding other SSDs with authigenic origins, such as pedogenic, mechanic or biologic triggers. The vertical and temporal occurrence along the study succession of these last SSDs is considered in discussion below. On the basis of lithology, morphology and size of soft-sediment deformation structures, four different types are established: clastic dykes and sills, load

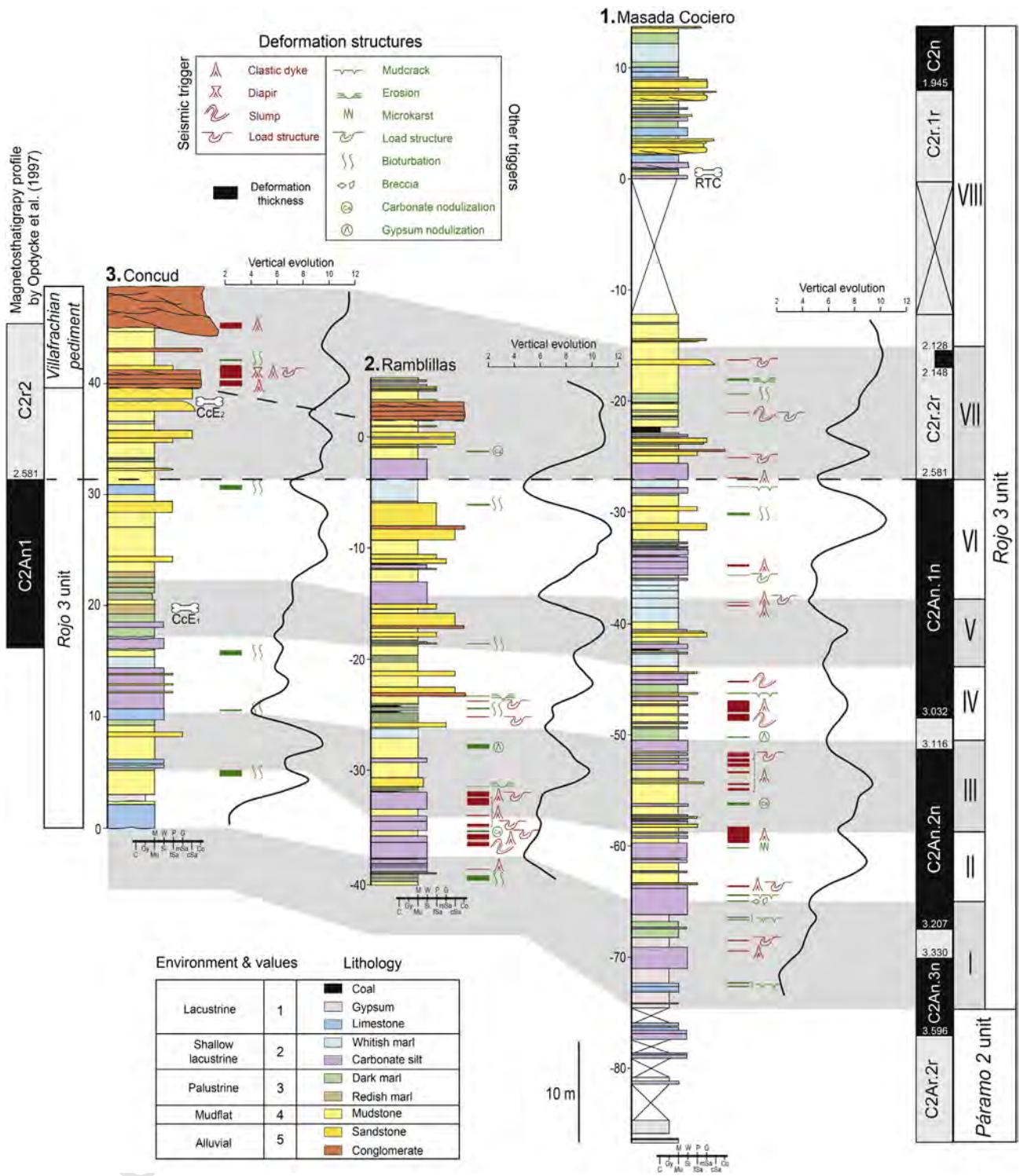


Fig. 6. Correlation of stratigraphic profiles and SSDs along the Conclud-Teruel Residual Basin. The sub-units for the Rojo 3 unit have been defined through vertical trend of sedimentary facies.

524 structures, slumps and diapirs (Fig. 6). We will distinguish well core and
 525 outcrop examples since our descriptions are strongly dependent on the
 526 scale of the available observations.

527 6.1. SSDs morphology

528 6.1.1. Clastic dykes

529 Clastic dykes and dyke-sill complexes appear six times in the
 530 Ramblillas well core. They show variable shape in 2D section, but always

531 have a more or less elongated cylindrical 3D morphology. Conduits are
 532 dominantly vertical and show sharp contacts with the surrounding
 533 materials.

534 Dykes in core examples are filled by structureless siltstone, silty
 535 sandstone and fine-grained sandstone. The host sediments are commonly
 536 distorted and folded upwards close to the conduit boundaries
 537 (Fig. 8b,d). The size of the vertical conduit is variable, ranging from 0.1
 538 to 1 m in height. Isolated and nearly vertical conduits occur in alternat-
 539 ing layers of siltstone and silty sandstone (Fig. 8b). Dyke-sill complexes,

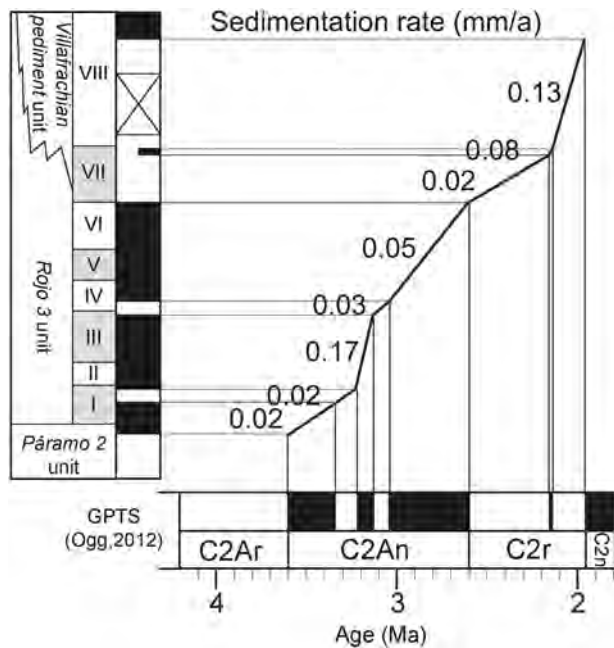


Fig. 7. Variation of sedimentation rate along the Masada Cociero profile.

consisting of vertical, inclined and horizontal conduits, are characteristic of mudstone-siltstone alternations (Fig. 8d). At their upper terminations, some dykes show convex morphologies (under mudstone beds) that slightly deform the overlying fine-grained laminae, while others have upward-widening funnel shapes. Source beds of the clastic dykes always show homogenized texture (Fig. 8c).

Dykes recognized at outcrop (two beds at the uppermost alluvial-lacustrine deposits of the Conclud section) are 0.45 to 0.5 m in height and show a laterally and vertically variable length. The upward-directed injections are developed in fine-grained sandstone, siltstone and conglomerate alternations and show irregular morphologies: they are often not vertical (Fig. 9a, b). In some dykes (Fig. 9a), the conduit is filled by coarse-grained reddish siltstone with floating gravels and deforms the adjacent coarse-grained sandstones, which show upward folded lamination. Other dykes only involve coarse-grained sandstones and conglomerates (Fig. 9b). Here, the conduit is filled by sandstone with dispersed gravels and cuts conglomerate beds, deforming them along upward-oriented tight folds (Fig. 9b). Close to the dyke borders, some pebbles have their major axis sub-parallel to the dyke (Fig. 9a,b). The dykes always end upwards at an erosional surface, overlain by undeformed sediments made up of channeled deposits with trough cross-bedding (Fig. 9a) or tabular well stratified gravel bodies with imbricated pebbles (Fig. 9b). Source beds of the clastic dykes always show a massive texture and vertically oriented clasts.

6.1.2. Load structures

In the Ramblillas well core we have recognized four deformed beds with load structures. They have variable heights, from a few centimeters to 0.5 m, but their total length is unknown because their size usually exceeds the diameter of the well log (Fig. 8a,c). They have been recognized as deformed interfaces between two sedimentary units with different lithology or grain-size and are represented by undulations with slight to tight folds with concave/convex morphologies. The overlying unit is made of sandstones or coarse-grained siltstones, while the underlying unit shows a finer grain size (siltstones and mudstones - Fig. 8a,c). In large load structures developed in silty materials, the internal lamination is curved following the structure morphology and, only in the core of the load-structure, laminae are irregularly deformed (Fig. 8c).

In the case of the small-scale load structures, several load casts separated by irregular flame structures can be recognized (Fig. 8a). Locally, the upper sediment moves downwards forming isolated drop-shaped bodies (pillow structures that are a few millimeters in width) in the lower sediment (Fig. 8a).

In the Conclud outcrops, large-scale load-structures (more than 0.3 m in length) are associated only with diapirs (see below) in a sandstone-dominated portion of the succession (Fig. 9d).

6.1.3. Diapirs

These structures have only been recognized in a 1.20 m-thick sandstone body in the Conclud outcrops. The deposits are made up of alternations of fine- to medium- and coarse-grained sandstone with trough cross-bedding. Several diapir structures occur, reaching a maximum of 0.42 m in height and 0.30 m in length (Fig. 9c). The term diapir is here used to describe dome-shaped SSDs that arch the overlying laminae without breaking them. In the upper part of the structures, the primary sedimentary lamination is well preserved but shows convexity, regardless of the grain size. In general, they represent symmetrical antiformal folds with angular hinge. The lower zones are made up of fine-grained sandstones, which are massive or show irregularly deformed laminae. Occasionally, some diapirs exhibit a mushroom geometry related to load structures, while others are truncated by an overlying erosional surface (Fig. 9d).

6.1.4. Slumps

Only one 0.40 m thick slump sheet has been recognized in the Ramblillas well core from -36.90 m to -36.50 m (Fig. 10). It involves alternations of grayish and whitish carbonate laminae, brown silts and yellowish coarse-grained silts. Contractural structures such as overturned folds have been recognized (consistent with a single lateral flow direction) even though their size exceeds the well core diameter. A completely distorted bed with folded dykes (brown silty material) appears at the lower part of the slump sheet (Fig. 10). Brown muddy silts with aligned fragments of whitish carbonate and grayish silts picks out a consistently oriented overturned fold (central part of Fig. 10). The uppermost complexly contorted and inclined lamination of grayish silts and mudstones also defines an overturned fold (Fig. 10).

6.2. Causes of deformation

The detailed description of soft-sediment deformation structures allows us to interpret the mechanism of deformation. Liquefaction is responsible for deformation of levels that preserve primary lamination (see Owen and Moretti, 2011). In both load-structures and laminae sets that are passively curved and/or broken by deformation of the adjacent soft-sediments, primary lamination is severely deformed, folded and/or disrupted but is always well recognizable. Fluidization is chiefly recorded by massive textures and upward-directed water-escape structures. Homogenized sediments in the clastic dykes and diapir structures are the result of elutriation of particles from a source bed during fluidization, when water and fluidized particles move upwards deforming the overlying sediments. In the well logs and outcrops, we have often observed the result of a selective-partial fluidization, in which only fine-grained particles made up the upward-directed portions of dykes and diapir structures. Slump sheets are the result of plastic and pseudoplastic deformation in soft-sediments. Being the result of re-sedimentation and/or slide events, the effects of the initial deformation are not recognizable.

The driving-force system (Owen, 1987; Owen et al., 2011) that is responsible for the final morphology of the described Pliocene-Quaternary deformed beds can be summarized as follows: i) load-structures form, after liquefaction, as a result of initial unstable density gradient systems or unequal loading distribution; ii) dykes and diapir structures form after fluidization, where the flow reaches a barrier or

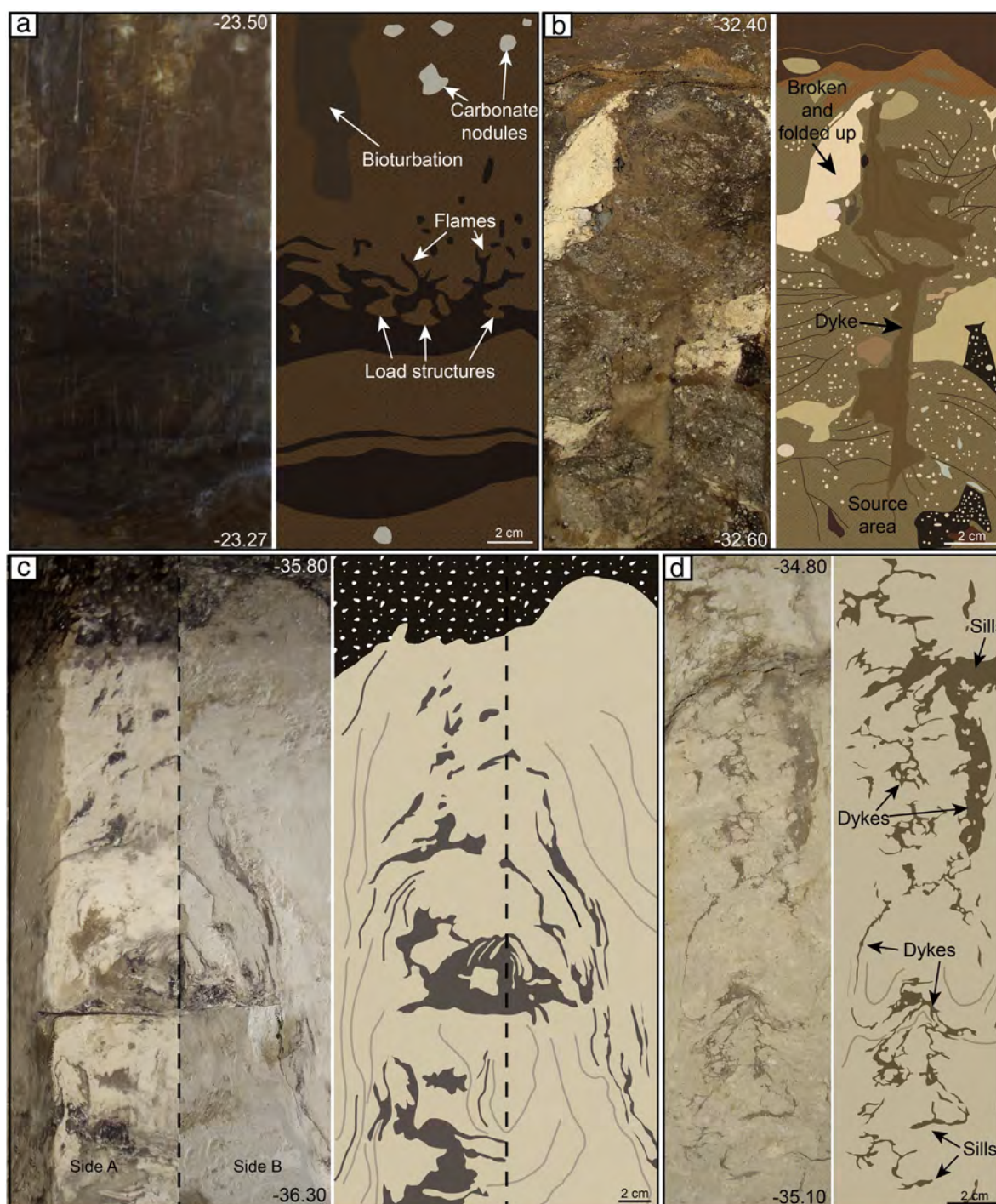


Fig. 8. (a) Load structures (load casts and small pillows) in a centimeter-scale bed, developed in pale-brown and dark-brown silts. Note the presence of bioturbation and carbonate nodules. (b) Clastic dyke: single vertical conduit filled with fine-grained silts and crossing surrounding heterolithic materials (mudstones, limestones and coal). Source bed is shown. (c) Large load-structure only visible between two perpendicular core sections (white silts and brown mudstones). (d) Complex of vertical, inclined and sub-horizontal (sill) dykes related to liquefaction of the brown silty material.

639 a sharp decrease in permeability; and iii) slump sheets are induced by
640 gravitational instability of a sedimentary body that undergoes liquefac-
641 tion, fluidization or loss of shear strength.

642 The interpretation of the trigger mechanism of SSDSs can be often
643 very difficult since many agents can produce very similar morphology
644 (e.g. Dzulyński and Walton, 1965; Lowe, 1975; Eissmann, 1994; Tuttle
645 et al., 2002; Montenat et al., 2007; Van Loon, 2009). Nevertheless,
646 reliable interpretations can be obtained by considering the entire data
647 and results arising from facies analysis and detailed description of

SSDSs (e.g. Obermeier et al., 1985; Guiraud and Plaziat, 1993; Moretti, 648
2000; Owen and Moretti, 2008; Alfaro et al., 2010; El Taki and Pratt, 649
2012). An exhaustive discussion on how to distinguish seismically- 650
induced SSDSs from aseismic ones in fluvial-lacustrine successions is 651
contained in Moretti and Sabato (2007), while the criteria for 652
recognizing seismites in well logs were systematized by Ezquerro 653
et al. (2015). 654

The effects of liquefaction and/or fluidization processes on load- 655
structures, dykes and diapir structures of the Pliocene–Quaternary 656

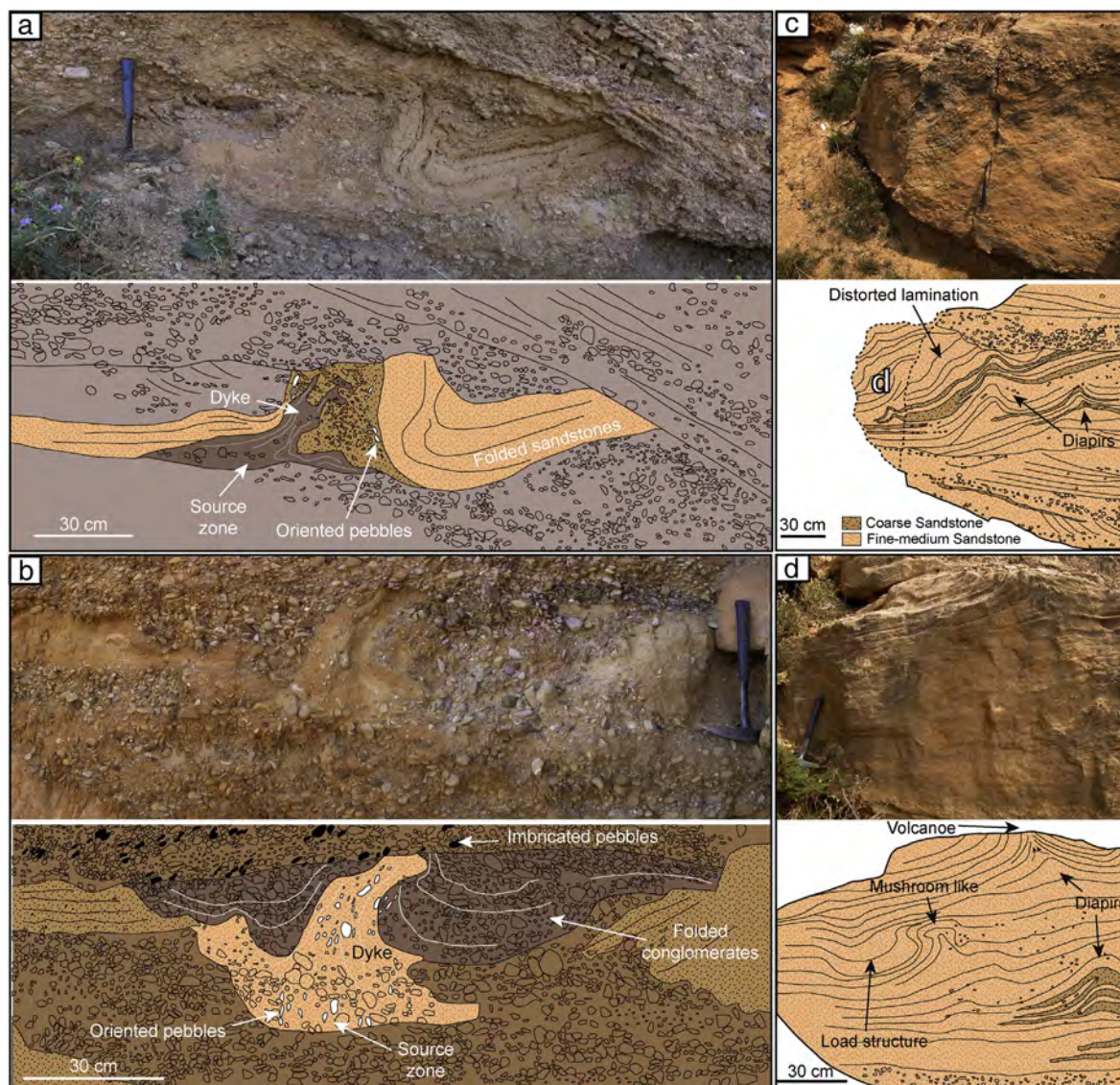


Fig. 9. (a) Large clastic dyke: single vertical conduit filled with fine-grained materials and crossing and deforming a sandstone bed. Source bed and oriented pebbles are shown. (b) Large clastic dyke: single vertical conduit filled with fine-grained materials and crossing and deforming the surrounding conglomerate. Source bed and oriented pebbles are shown. (c) Diapirs and load structures developed in a complete deformed sandstone channel body.

657 deposits of the Jiloca Basin can be interpreted as seismically-induced
 658 since it is possible to exclude the action of other trigger mechanisms.
 659 Some mechanisms that are able to induce liquefaction and fluidization
 660 are not compatible with the described facies associations such as wave
 661 action or sudden variations of the water-table depth. Furthermore, the
 662 palustrine-lacustrine facies described in the two studied well logs do
 663 not show evidence of storm-wave action, overloading or unequal loading
 664 processes. The only authigenic factor that could be invoked is
 665 overloading by gravel-dominated alluvial beds of Fig. 5 (Concud out-
 666 crops). Nevertheless, calculations and experimental analog models
 667 (Moretti et al., 2001) show that the height of deformation (h) in a sub-
 668 strate induced by the instantaneous deposition of a bed is more or less
 669 similar to its thickness (H). In our field examples, the overlying sedi-
 670 ments are always well-laminated sands and gravels with imbrication,
 671 indicating deposition from tractive flows and excluding the possibility
 672 of rapid mass flows and its overloading effects. We also interpret the
 673 described slumps as seismites since they occur in almost-flat environ-
 674 ments and in the absence of transient slopes associated with large-
 675 scale traction bedforms (Field et al., 1982; Spalluto et al., 2007; García-

Tortosa et al., 2011; Mastrogiacomo et al., 2012; Alsop and Marco, 676
 2013). 677

678 6.3. Lateral and vertical distribution of SSDSs 679

680 Once described and interpreted, the SSDSs recognized in the
 681 Ramblillas and Concud profiles can be combined with the results from
 682 Masada Cociero (Ezquerro et al., 2015) in order to analyze their overall
 683 distribution in the studied area. Fig. 6 shows, for each studied profile,
 684 their location and type of SSDSs, as well as the interpreted (seismic or
 685 non-seismic) origin. 686

687 The Masada Cociero profile contains most of the SSDSs recognized.
 688 Almost systematically, 1 or 2 non-seismic structures appear within
 689 each sub-unit in this profile, independently of the involved lithology.
 690 An exception is recognized in the evaporite facies of the two lower, I
 691 and II sub-units, where mudcrack levels are concentrated. Seismically
 692 induced SSDSs are also present in every sub-unit (usually, 2 or 3 struc-
 693 tures). Nevertheless, a group that involves 12 structures developed in
 694 heterolithic facies is easily recognizable in sub-units III and IV. 695

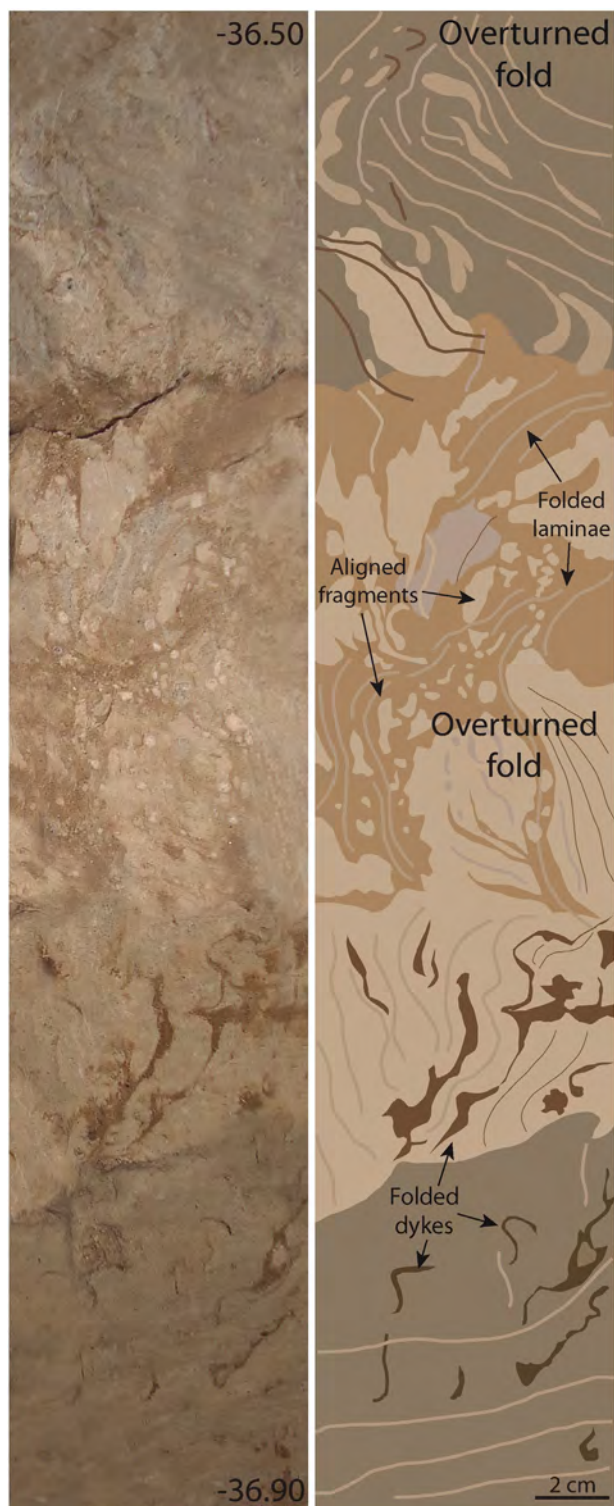


Fig. 10. The thickest slump sheet in the Ramblillas well core. Overturned folds deform white, grayish and brown carbonate silts laminae.

In the Ramblillas profile, non-seismic SSDSs show a similar vertical distribution that in Masada Cociero, with 1 or 2 deformation levels per sub-unit. However, seismically induced structures have been only recognized in the lower sub-units (II, III and IV sub-units), with a cluster of 10 seismically-induced beds in laminated silty facies of sub-units II and III.

The Concud profile, which was totally logged at outcrop and exhibits the most massive sediments, has the minimum number of recognized SSDSs. Non-seismic deformations correspond exclusively to bioturbation traces (1 or 2 structures per sub-unit) that were able to produce extensive distortion of deposits. The only 3 seismically induced SSDSs recognized are clustered within a clastic alternation at the top of the profile (sub-unit VII, *Villafranchian pediment* unit).

In the Concud-Teruel Residual Basin, most types of aseismic deformation structures appear *quasi* equally vertical spaced in the three studied sections and affect any sedimentary facies. According to our correlation model, they appear at similar stratigraphical positions, suggesting their lateral continuity. By contrast, seismites have a more irregular vertical distribution in different sections. Their lateral correlation is generally difficult where they appear isolated, while this becomes easier for seimite clusters (especially in sub-unit III of Masada Cociero and Ramblillas profiles). In sub-unit VII, lateral overlapping between the SSDSs groups of Concud and Masada Cociero profiles can be recognized. For sub-units I, V and VI, seismites only appear in the Masada Cociero profile.

After achieving the overall correlation of SSDS levels, a number between 29 and 35 seismic deformed levels have been computed for the whole stratigraphic section. For 6 deformation levels, we admit a seismic origin, but not undeniable correspondence between profiles. Such an inventory of seismites represents a valued paleoseismic archive for the time interval (between ~3.6 and ~1.9 Ma).

7. Discussion

7.1. Spatial and temporal occurrence of seismic and non-seismic SSDSs

The distribution of observed seismically-induced SSDSs is strongly heterogeneous along the different borehole and surface records (Figs. 3, 6): they occur along the whole well log at Masada Cociero, are concentrated at the lower part of the Ramblillas well log, and are virtually absent in surface profiles except for the uppermost part of the Concud profile.

As a first approach, the overall frequency of seismites decreases from profile 1 (Masada Cociero) to 2 (Ramblillas) and 3 (Concud), as the distance from the Concud Fault increases, which is consistent with a simple attenuation law from the fault that constitutes the main seismogenic source in the area. This evinces that the magnitude threshold commonly proposed for occurrence of seismic SSDSs ($M_w \sim 5$) is meaningful only for the epicentral area. Even though this magnitude could have been exceeded, the probability of seimite occurrence would diminish as the epicentral distance increases.

On the other hand, we should not forget that SSDSs distribution is also controlled by the observation scale and involved sedimentary facies (e.g., Alfaro et al., 1997; Rodríguez-López et al., 2007; Liesa et al., 2016), which can explain the scarcity of SSDSs in the westernmost, Concud profile. Outcropping conditions seem to have inhibited the recognition of SSDSs under decametric-scale, so that only a few, large SSDSs could be observed in this profile. Data from Concud correspond to more proximal, alluvial facies, showing predominance of massive, coarse clastic sediments, with low lithological variety and arranged in thicker beds. This makes it more difficult to develop conserve and recognize SSDSs, in contrast with those of palustrine-lacustrine areas.

Nevertheless, other pieces of evidence support the tectonic control on SSDS distribution. The clear difference between both well logs at the central-upper part of the succession (abundant seismically-induced SSDSs in Masada Cociero, virtual absence in Ramblillas) clearly supports the idea that most seismic events that occurred during chrons C2An.2n and C2r produced SSDSs only within a distance of less than 1 km from the fault trace. Since this did not occur for events during the previous chron C2An.3n, we can

infer that the magnitude of paleoseisms within the period C2An.2n was greater than during C2An.3n. Afterwards, a number of large paleoseisms again occurred during C2r, which were recorded by large-scale SSDSs in deposits of the *Villafranchian pediment* unit in spite of its unfavorable lithology.

Through the overall stratigraphic succession, although broadly distributed (2–3 structures per sub-unit, in average), seismites appear clustered, mainly in sub-units III and IV in Masada Cociero and sub-units II and III in Ramblillas. Both groups coincide with heterolithic or laminated facies, which points again to a lithological control. But they are also linked to an episode of increased sedimentation rate (0.17 mm/a, Fig. 11), which suggests close relationship with accelerated tectonic subsidence, therefore increasing activity of the Concul Fault. We exclude the climatic control on the sedimentation rate changes due to the fact that the succession becomes thicker towards the fault. However, a period of high sedimentation rate, between 2.128 and 1.945 Ma (Fig. 11), shows very scarce occurrence of SSDSs. We interpret this in terms of poor observation conditions, since this time span is entirely represented by the upper, surficial part of the Masada Cociero profile and the observation gap below. A similar case has been described in the Early Cretaceous Villanueva de Huerva Fm. in the Iberian Basin (Soria et al., 2013), where the maximum development of slumping coincides with episodes of tectonically-induced high sedimentation rate (evinced by thicker cycles of lake expansion-retraction related to precession Milankovitch cycle).

With respect to non-seismic deformations, these show a quite distinct distribution pattern. They appear regularly spaced in the studied series and are associated with any sedimentary facies. Such features, as well as their lateral arrangement at similar stratigraphical positions, point to cyclically pedogenic, mechanical or biological triggers that induced authigenic processes in the basin. Such processes, and hence the vertical distribution, might be ultimately controlled by climatic cycles (e.g. De Wet et al., 1998; Luzón et al., 2002; Abels et al., 2009; Soria et al., 2013). An exception to the regular occurrence of non-seismic SSDSs is the cluster of mudcrack levels in evaporite facies (sub-units I and II) in the Masada Cociero profile. These mudcracks probably developed in frequent desiccation episodes in such a saline environment.

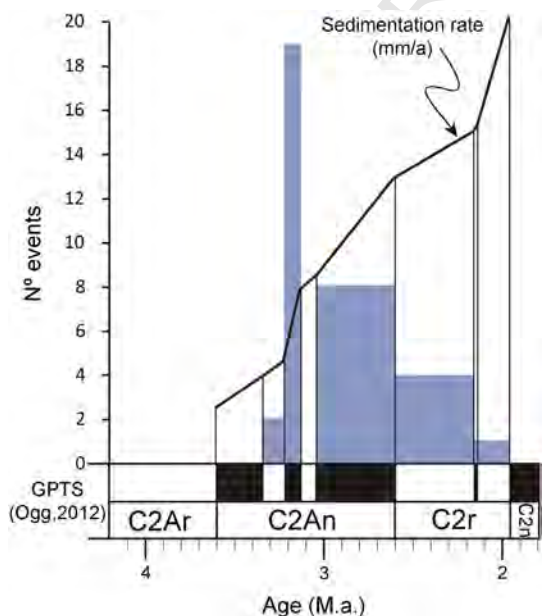


Fig. 11. Sedimentation rate vs. number of seismic events for each chron.

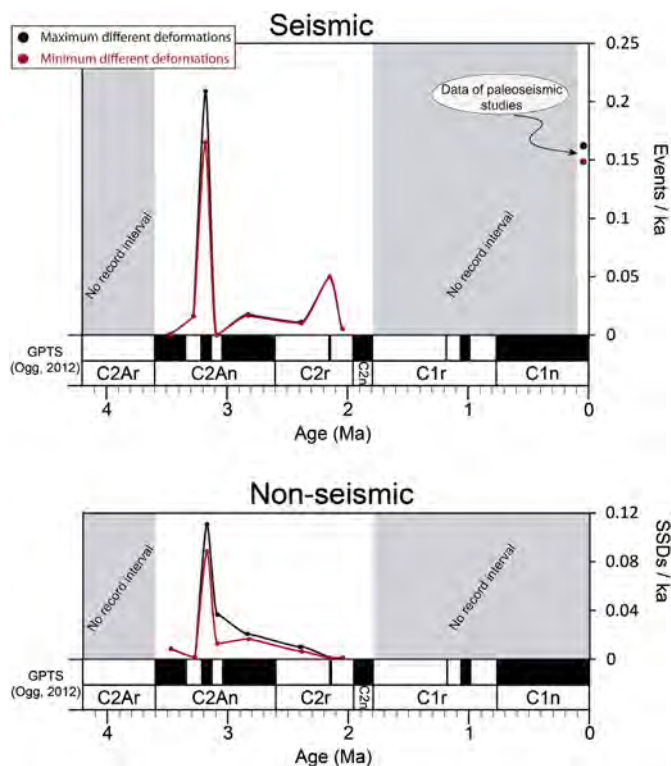


Fig. 12. Frequency (inverse of the apparent recurrence period in ka) of seismic events ($M \geq 5$) and non-seismic SSDSs during the studied time interval.

7.2. Insights into the apparent recurrence period of paleoseisms and its time variation

After correlating every seismically-induced SSDSs level through the studied profiles, we have computed the total paleoseismic record and calculated the apparent frequency of paleoseismic events for each time slice represented by either a chron or a sub-chron (Fig. 12). Such frequency usually ranges from 0.01 to 0.02 events/ka, except for two periods (sub-chrons C2An.2n and C2r.1n), in which frequency increases up to 0.16 and 0.05, respectively, coinciding with (i) the high concentration of small-scale SSDSs in the lower part of both boreholes (paleoseisms that produced SSDSs within a distance exceeding 1 km), and (ii) large-scale SSDSs in coarse clastic sediments at the upper part of Concul (therefore, also representing relatively strong seisms).

Both periods with high paleoseismic frequency are quite short. One could suspect that such coincidence perhaps represents an artifact caused by biased sampling. Nevertheless, such SSDS ensembles represent sharp clusters in time but not in the thickness of the sedimentary succession. We have explained how both coincide with periods of high sedimentation rate; therefore, their correspondence with periods of high tectonic subsidence, and hence their tectonic control, is proved.

From results compiled in Fig. 12, we have computed the corresponding apparent recurrence periods (represented in the figure as frequency of seismicity). After computing 35 seismic events between ~3.6 and ~1.9 Ma, an average recurrence period of ~47 ka is calculated for the whole succession. This value is close to the first estimation by Ezquerro et al. (2015). The background value is between 56 and 108 ka, considering the maximum and minimum different SSDSs, while periods with high frequency of seismic pulses represent around to 4.8 to 6.1 ka.

832 7.3. Comparison with Pleistocene paleoseismicity

833 After calculating those *apparent recurrence periods* of paleoseisms for
834 a number of time intervals within the Late Pliocene–Early Pleistocene, it
835 seems pertinent to compare them with the recurrence times obtained
836 from trench analysis in Late Pleistocene deposits of the same area to
837 provide a wider temporal viewpoint for assessing the activity pattern
838 of the Concul Fault.

839 Briefly, we have explained how the average recurrence period of
840 large earthquakes (*characteristic earthquakes*) for the last 74 ka has
841 been calculated at between 7.1 and 8.0 ka, based on identification of
842 eleven paleoseismic events in five trenches along the Concul Fault
843 (Lafuente et al., 2014; Simón et al., 2015). This range approaches the *ap-*
844 *parent recurrence period* (4.8 to 6.1 ka) calculated for the time interval
845 with the maximum frequency of seismic SSDSs. i.e. the sub-chron
846 C2An.2n. It is noteworthy that the duration of this sub-chron (91 ka)
847 is of the same order as the time span covered by trench studies
848 (74 ka), which allows us to rule out any bias related to representativ-
849 ness of the computed period.

850 Going deeper into this issue, we should remember that the threshold
851 commonly proposed for occurrence of seismic SSDSs ($M_w \sim 5$) is re-
852 markably lower than that inferred for the characteristic earthquake at
853 the Concul Fault ($M_w = 6.5–6.6$), so that our apparent recurrence pe-
854 riod from SSDSs is expectable to be shorter than the average recurrence
855 period of the characteristic earthquake. The 500-year seism for this
856 fault, calculated by interpolating between historic-instrumental and
857 paleoseismic records, is $M \sim 5.3$ (Simón et al., 2014). Therefore, 0.5 ka
858 would represent a more realistic value for the expectable recurrence pe-
859 riod obtained from seismites.

860 Nevertheless, paleoearthquakes below the *characteristic magnitude*
861 are likely not linked to activation of the entire Concul Fault surface.
862 Therefore, they did not involve surface rupture, and their foci could be
863 located quite far from our studied boreholes (up to ~20 km, according
864 to the length and depth of the fault). In such a case, the studied
865 boreholes would be out of the epicentral area, and we should not expect
866 every seism of that magnitude to be recorded in them. In summary, our
867 apparent recurrence period (4.8–6.1 ka), bracketed between the
868 recurrence period corresponding to the SSDSs threshold magnitude
869 (~0.5 ka) and that of the characteristic earthquake of the closest
870 seismogenic fault (7.1–8.0 ka), can be considered as a consistent
871 result.

872 After that successful comparison between their respective
873 paleoseismic patterns, we can infer that both the Late Pleistocene (and
874 Holocene?) and the sub-chron C2An.2n within the Late Pliocene
875 (3.207–3.116 Ma) were periods of high activity along the Concul
876 Fault history. The curve of sedimentation rate in Figs. 7, 11 provides a
877 framework for assessing such temporal pattern of activity, since it can
878 be interpreted as a proxy of variation of tectonic subsidence with
879 time. Values of sedimentation rate for the Late Pliocene should be
880 considered as slightly lower than those of tectonic subsidence:
881 sedimentation is constrained to the Teruel–Concul Residual Basin, but
882 sedimentological features of the infill do not evince any noticeable
883 positive relief at its margins (Ezquerro et al., 2015). In this sense, the
884 coincidence between both periods of high activity is also remarkable:
885 the maximum sedimentation rate recorded in the Masada Cociero
886 succession (0.17 mm/a) corresponds to the sub-chron C2An.2n and
887 approaches the average slip rate (0.29 mm/a) calculated for the last
888 74 ka (Simón et al., 2015).

889 These periods of high activity would have alternated with periods
890 of low activity (*apparent recurrence period* of seismic events in the
891 range of 56 to 108 ka; sedimentation rate as low as 0.02 mm/a, see
892 Figs. 7, 11), resulting in average values, for the overall studied time
893 interval, of 47 ka and 0.06 mm/a, respectively. Such alternation, at
894 a time scale of the order of 10^5 years, is modulated by a similar
895 fluctuation at a more detailed scale (10^4 years), as shown by the
896 slip history of the Concul Fault during the Late Pleistocene. The latter

is characterized by alternating periods of faster slip (74.5 to 60 ka BP, 897
0.53 mm/a; 21 to ca. 8 ka BP, 0.42 mm/a) and slower slip (60 to 21 ka 898
BP, 0.13 mm/a) (Lafuente et al., 2014; Simón et al., 2015). This 899
suggests a *fractal* pattern in the occurrence of seismic events through 900
time, with clusters that could be identified at every time scale, 901
depending on the observation time window. Instrumental earthquake 902
swarms would be the shortest and most recent example of such seismic 903
clusters indeed. 904

From the methodological point of view, we should notice the coinci- 905
dence of time occurrence patterns recognized for peaks of paleoseismic 906
activity in the studied area from both primary evidence in trenches and 907
secondary evidence in boreholes. This gives support to the notion of the 908
apparent recurrence period as defined by Ezquerro et al. (2015). At least 909
for those calculated from SSDS inventories collected in borehole logs 910
close to seismogenic faults, *apparent recurrence periods* are comparable 911
to actual recurrence times of paleoearthquakes (those exceeding 912
the SSDSs magnitude threshold and approaching the *characteristic* 913
magnitude). 914

8. Conclusions 915

A high number of SSDSs (35 of seismic origin and 28 of non-seismic 916
origin) have been identified in three sections (Concul, Ramblillas and 917
Masada Cociero), logged from boreholes and outcrops in Late Pliocene– 918
Early Pleistocene deposits of the Teruel–Concul Residual Basin, close to 919
the Concul normal fault. They belong to a variety of types, such as clastic 920
dykes, load structures, diapirs, slumps, nodulizations or mudcracks. 921

Timing of seismic and non-seismic SSDSs has been initially 922
constrained from biostratigraphic data (mammal sites) and a previous 923
magnetostratigraphic profile (Opdyke et al., 1997), then substantially 924
refined from a new magnetostratigraphic study at Masada Cociero 925
site. The overall stratigraphic section and the recorded SSDSs cover a 926
time span between ~3.6 and ~1.9 Ma. 927

Non-seismic SSDSs are relatively well-correlated between sections, 928
while seismic ones are poorly correlated, except for several clusters of 929
structures. After achieving the correlation, a number between 29 and 930
35 seismically deformed levels have been computed for the overall 931
stratigraphic section. 932

Main controls on the lateral and vertical distribution of the SSDSs 933
are: i) origin (either seismic or non-seismic) of deformation structures; 934
ii) distance to seismogenic source (the Concul Fault); and iii) sediment- 935
ary facies involved in deformation. 936

The paleoseismites are broadly distributed along the Upper 937
Pliocene–Lower Pleistocene Teruel–Concul Residual Basin, but their 938
record is more complete near the Concul Fault, i.e. near the source 939
for paleoseisms and where the sedimentary facies, ultimately 940
controlled by tectonic subsidence, was also more suitable for their 941
development. 942

In the overall stratigraphic section (~3.6 to ~1.9 Ma), seismites show 943
an apparent recurrence period of 56–108 ka. Clustering of eighteen seis- 944
mic SSDSs levels within the chron C2An.2n (3.207 to 3.116 Ma) reveals 945
much higher paleoseismic activity, with an apparent recurrence period 946
of 4.8 to 6.1 ka. Increase in sedimentation rate, and hence tectonic sub- 947
sidence, during this interval reinforces the scenario of SSDSs triggered 948
by the Concul Fault activity. 949

The Late Pliocene–Early Pleistocene activity of the Concul Fault 950
shows a similar behavior to that for the Late Pleistocene (last ca. 74 ka 951
BP), with alternating periods of faster and slower slip. The difference 952
is the time scale of the recognized fluctuations: of the order of 953
 10^5 years for the Late Pliocene–Early Pleistocene, and 10^4 years for the 954
Late Pleistocene. 955

In the study area, time occurrence patterns recognized for peaks of 956
paleoseismic activity from secondary evidence in boreholes are similar 957
to those inferred from primary evidence in trenches. This gives support 958
to the notion of *apparent recurrence period* as defined by Ezquerro et al. 959
(2015). At least for those calculated from SSDS inventories collected in 960

borehole logs close to the seismogenic faults, *apparent recurrence periods* are comparable to actual recurrence times of large paleoearthquakes.

Q10 Uncited reference

Alfaro et al., 1995

Acknowledgments

We would thank J.J. Díaz-Martínez and G. Owen for their valuable comments and suggestions which have permitted to improve the final version of our manuscript. Special thanks to Cristina García-Lasanta for helping us during the paleomagnetic fieldwork and Elisa Sanchez and the laboratory of the University of Burgos. Research has been supported by project CGL2012-35662 of the Spanish Ministerio de Economía y Competitividad-FEDER, as well as by the Aragón regional government (“Geotransfer” and “Análisis de Cuencas Sedimentarias Continentales” research groups). L. Ezquerro benefited from a FPI grant (BES-2010-031339) of Spanish Ministerio de Economía y Competitividad.

Appendix A. Paleomagnetism

A.1. Sampling and laboratory procedures

Paleomagnetic sampling (one sample each 0.5 m, except in the sedimentary gaps) was performed using both, standard drilling techniques and soft material extraction procedures. In total, 160 standard paleomagnetic cores were obtained; 26 samples come for the Masada Cociero outcrop and 134 samples were taken in the well core obtained with an extractor of soft materials. Samples were consolidated later in the laboratories of the University of Zaragoza using Sodium silicate (50% solution) and Aluminum cement (Pueyo et al., 2006).

Every standard sample gave 1–2 specimens and 263 of them were demagnetized in the laboratory (≈ 2 specimens per stratigraphic level in average out). Paleomagnetic measurements were taken at the laboratory of the Applied Physics Department of the University of Burgos (Spain). Stepwise thermal demagnetization was successfully applied to separate magnetic components in most samples. Different routines were used; steps every 50 °C at low temperatures (only until 400–550 °C) and every 20°–30 °C at the higher ones or, alternatively, increments of 50 °C up to 450 °C; increments of 25 °C up to 575 °C and 20 °C steps until the end (680 °C). Demagnetization routine was always designed to reach high temperatures by means of 18 steps. Measurements were done using a 2G superconducting cryogenic magnetometer and MMTD80A (by Magnetic Measurements Ltd) and TD-48 (by ASC Scientific Ltd) ovens.

Directions of the Characteristic remanent magnetization (ChRM) were fitted using the software VPD (Ramón and Pueyo, 2012 and Ramón, 2013) that allows the standard principal component analysis (Kirschvink, 1980) and the demagnetization circles technique (Bailey and Halls, 1984). Fisher (1953) statistics was applied to obtain spherical means using the stereonet program (Allmendinger et al., 2012).

A.2. Paleomagnetic stability

Isothermal remanent magnetization (IRM) acquisition curves outline the contribution of different magnetic mineral to the remanence, in relation to the lithological variety. The thermal demagnetization of the 3-components IRM (Lowrie's test, 1990) has helped us to characterize the different carriers of the magnetization. In carbonate, evaporate and withish rocks, magnetically soft mineralogy is predominant and is saturated at low magnetic fields. Hard mineralogy represented by phases of

high coercivity cannot fully ruled out but it displays a minor contribution in these samples (Fig. Appendix 1). In reddish mudstones and sandstones, the dominant contribution to the remanence is imposed by the hard mineralogy, mostly hematite. A frequent decay at 300 °C has also been observed attesting for the presence of iron sulfides in many lithologies, especially in organic rich levels and siltstones with high levels of organic matter. Many of the samples showing iron sulfides also shown remanences unblocking up to 550 to 600 °C. Red mudstones and sandstones unblock at higher temperature > 600 °C (Fig. 5). All these results point to magnetite as the main carrier of the remanence in the Masada Cociero, although iron sulfurs and hematite contributing to the remanence in some cases.

A.3. Re-orientation methodology

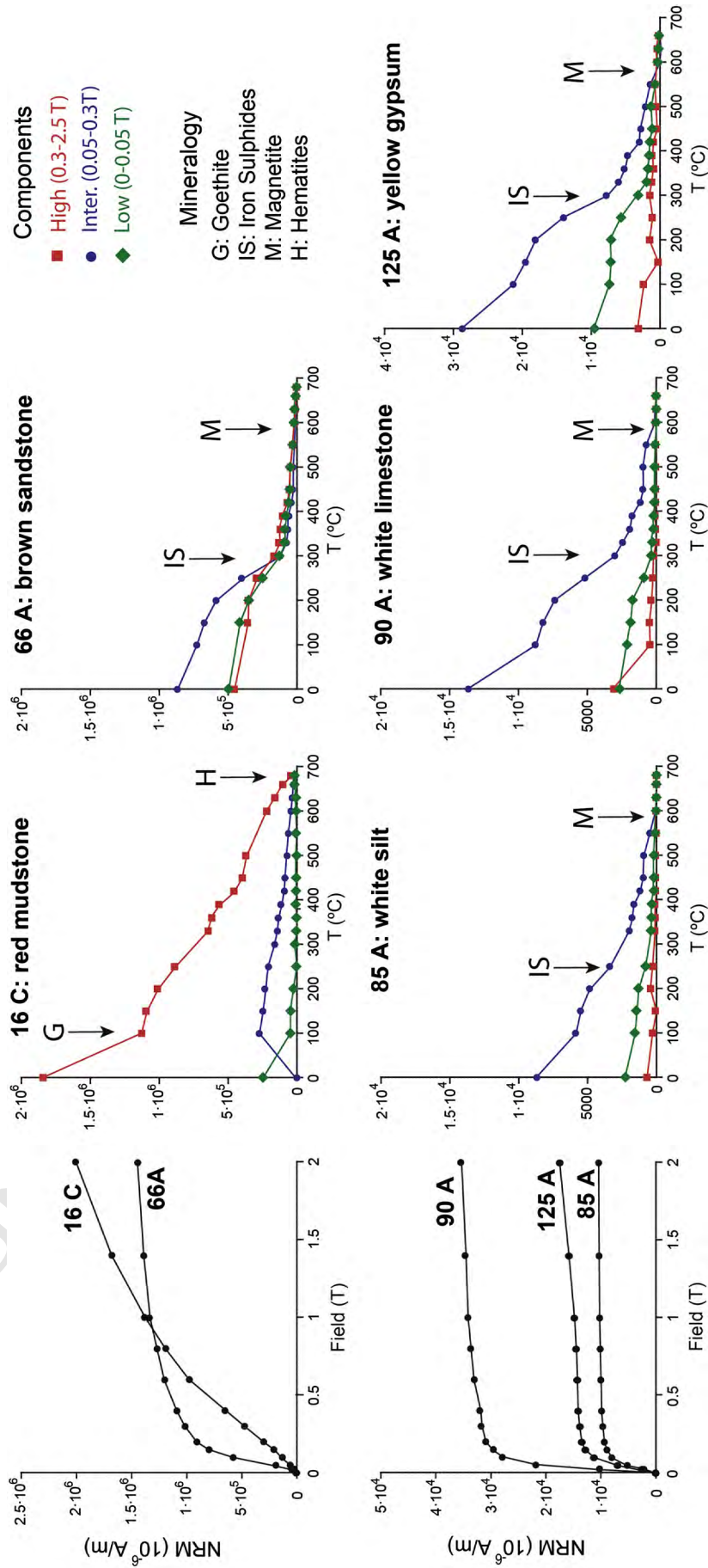
The samples coming from the well core have been extracted perpendicular to an arbitrary orientation line which is parallel to the well core axis, besides top and base of the section is known. Thus, each sample is perpendicular to the well core axis. In this way, a common reference system for all specimens is established, allowing for a direct comparison of their paleomagnetic data (Bleakly et al., 1985; Van Alstine et al., 1991; Van Alstine and Butterworth, 1993; Hamilton et al., 1995).

VRM has a declination -0.2829° W and an inclination 55.1873° using the field model WMM2015 (www.ngdc.noaa.gov) in the Concu location (latitude: 40.30° N, longitude: 1.15° W; elevation: 1.0 km over the mean sea level). The viscous component of most samples (Fig. Appendix 2) shows inclination values almost coincident to the expected present-day geomagnetic field (deduced from the NOAA's National Geophysical Data Center using the IGRF12-gufm1 model (Jackson et al., 2000), although the drilling orientation induces a slightly modification in the NRM and VRM orientations respect to the present day field (Fig. Appendix 3). Thus reorientation method can be applied.

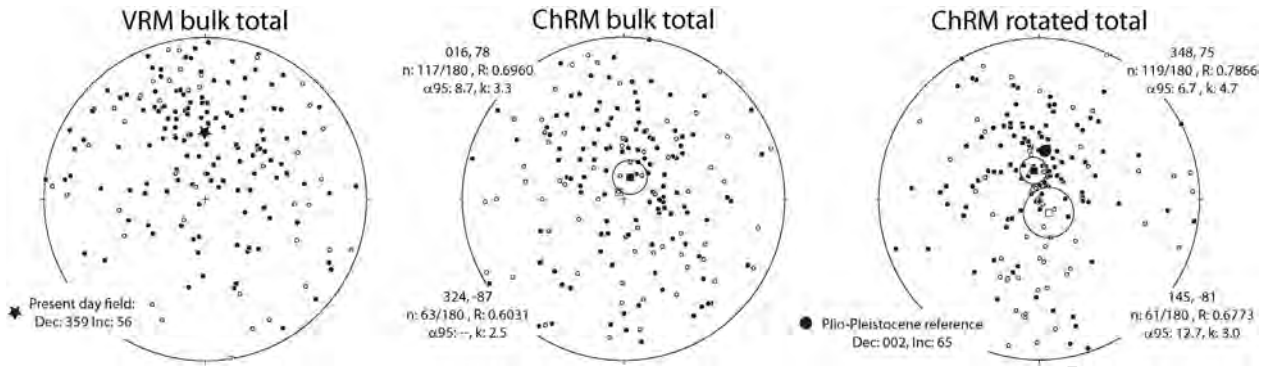
Once the amount of rotation between the initial direction and the true direction of the VRM is known, the ChRM have been jointly rotated to its probable orientation, giving the true orientation of the sample. Re-oriented magnetic data are approximately antipodal directions of normal polarity (upper hemisphere) with respect to reverse polarity (lower hemisphere); 348, 75 (α_{95} : 6.7° ; k: 4.7 and R: 0.7866) and 145, -81 (α_{95} : 127° ; k: 3.0 and R: 0.6773), which share a common true mean (Fig. Appendix 2). Besides, the combined mean vector in the lower hemisphere (173, 75; α_{95} : 6.8° ; k: 4.6 and R: 0.7866) falls very close to the expected Plio-Pleistocene reference direction (Dec: 002, Inc.: 65). This reference was deduced for the Masada Cociero location (Latitude: $55^\circ 9' 50''$ N, Longitude: $0^\circ 48' 5''$ W) using the Plio-Pleistocene poles of Iberia (Osete and Palencia, 2006).

A.4. Quality filter

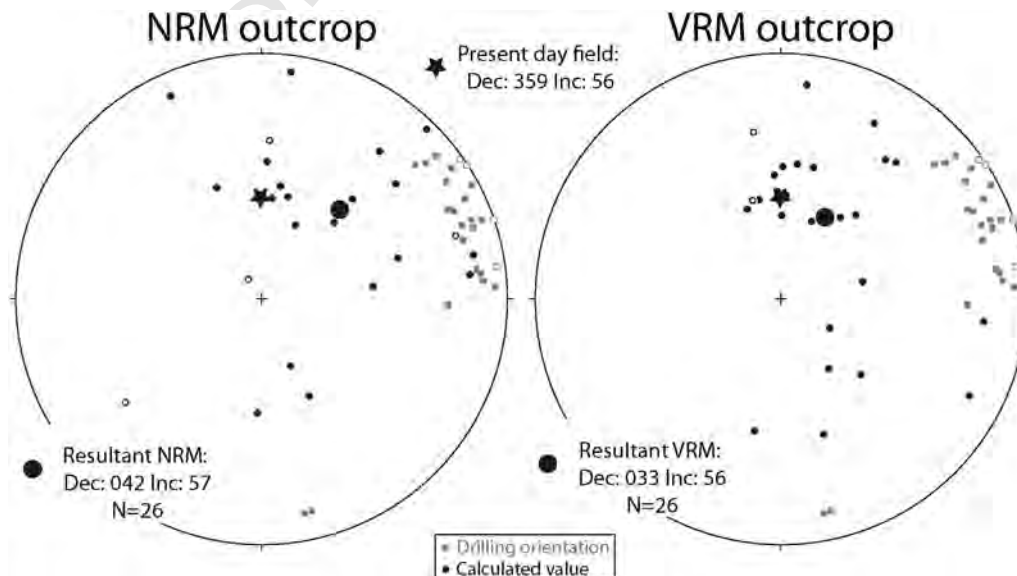
Samples from different classes are in similar proportions: 30% samples are class I, 40% samples class II and class III approximately represents a 30% of the dataset. Focusing only on directions used for building the LPS (classes I and II); $\approx 86\%$ of them display $MAD < 20^\circ$ and are characterized by more than 5 demagnetization steps in average (Fig. Appendix 4). Focusing only on directions used for building the LPS (classes I and II); $\approx 86\%$ of them display $MAD < 20^\circ$ and are characterized by more than 5 demagnetization steps in average. Some additional criteria were set up to define a magnetozone: i) two or more consecutive stratigraphic levels with the same polarity sign (VGP); ii) at least one level (usually more) must belong to the class I group; and iii) following the concept by Vandamme (1994) and Deenen et al. (2011), a $\pm 30^\circ$ cutoff for the VGP latitude around the equator helps removing undesirable noise.



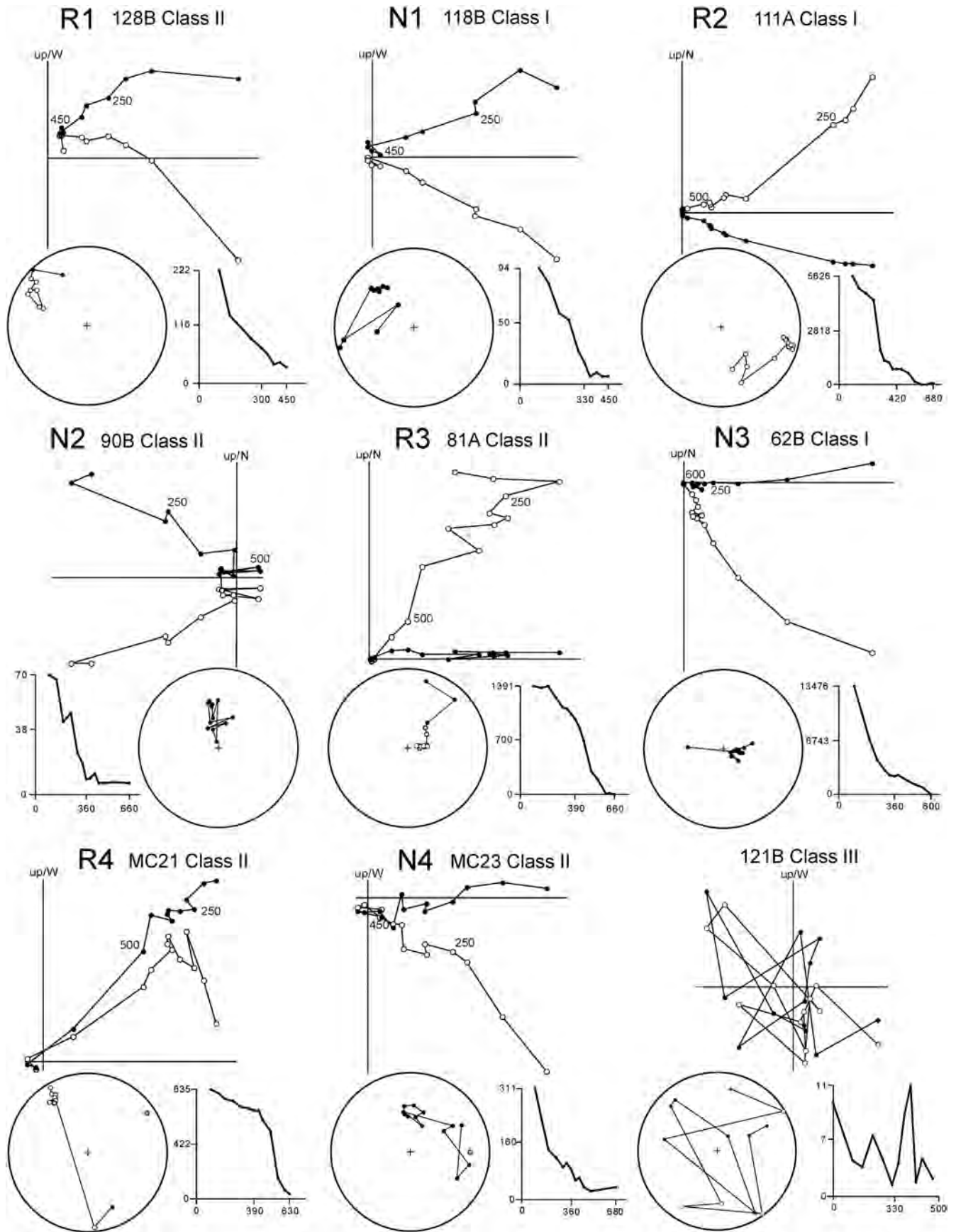
Appendix Fig. 1. IRM acquisition curves and thermal demagnetization results of a three-component lithologies samples. G, IS, M and H indicates the decay of remanence associated with Goethite, Iron Sulphides, Magnetite and Hematite, respectively.



Appendix Fig. 2. Characteristic directions from the Masada Cociero section in the stereonet. Only class I and II samples were used in these plots. VRM inclination is relatively closed to the present day field. VRM and ChRM data display an arbitrary distribution; ChRM after paleogeographic correction shows antipodality. Fisher (1953) means are also displayed.



Appendix Fig. 3. Drilling modifies the NRM and VRM orientations. Black symbols represent the NRM and VRM resultant of the samples and gray symbols imply the drilling orientation.



Appendix Fig. 4. Thermal stepwise demagnetization of the NRM; orthogonal diagrams from the Masada Cociero section. Displayed samples are evenly distributed along the studied profiles (local magnetozone number is shown for every diagram). Intensity decay curves in 10–6 A/m and stereographic projections. Gray circle in the stereonets represent the orientation of drilling. Diagrams derived from the VPD program (Ramón, 2013).

References

- 1080 Abels, H.A., Abdul Aziz, H., Ventra, D., Hilgen, F.J., 2009. Orbital climate forcing in mudflat
1081 to marginal lacustrine deposits in the Miocene Teruel Basin (Northeast Spain).
1082 *Journal of Sedimentary Research* 79, 831–847.
- 1083 Adrover, R., 1986. Nuevas Faunas De Roedores en El Mioplioceno Continental de la región
1084 de Teruel (España). Interés biostratigráfico Y paleoecológico. Instituto de Estudios
1085 Turolenses, Teruel (433 pp.).
- 1086 Adrover, R., Mein, P., Moissenet, E., 1978. Nuevos datos sobre la edad de las formaciones
1087 continentales neogenas de los alrededores de Teruel. *Estudios Geológicos* 34,
1088 205–214.
- 1089 Alcalá, L., Alonso-Zarza, A.M., Álvarez, M.A., Azanza, B., Calvo, J.P., Cañaveras, J.C., van Dam,
1090 J.A., Garcés, M., Krijgsman, W., van der Meulen, A.J., Morales, J., Peláez, P., Pérez-
1091 González, A., Sánchez, S., Sancho, R., Sanz, E., 2000. El Registro sedimentario y
1092 faunístico de las cuencas de Calatayud-Daroca y Teruel. Evolución paleoambiental y
1093 paleoclimática durante el Neógeno. *Revista de la Sociedad Geológica de España* 13,
1094 323–343.
- 1095 Alfaro, P., Doménech, C., Estévez, A., Soria, J.M., 1995. Estructuras de deformación en
1096 sedimentos del Cuaternario reciente de la Cuenca del bajo Segura (Alicante).
1097 Discusión sobre su posible origen sísmico. *Geogaceta* 17, 91–94.
- 1098 Alfaro, P., Moretti, M., Soria, J.M., 1997. Soft-sediment deformation structures induced by
1099 earthquakes (seismites) in Pliocene lacustrine deposits (Guadix-Baza Basin, central
1100 Betic cordillera). *Eclogae Geologicae Helveticae* 90, 531–540.
- 1101 Alfaro, P., Gibert, L., Moretti, M., García-Tortosa, F.J., Sanz de Galdeano, C., Galindo-
1102 Zaldívar, J., López-Garrido, T.C., 2010. The significance of giant seismites in the plio-
1103 Pleistocene Baza palaeo-lake (S Spain). *Terra Nova* 22, 172–179.
- 1104 Allen, J.R.L., 1986. Earthquake magnitude-frequency, epicentral distance, and soft-
1105 sediment deformation in sedimentary basins. *Sedimentary Geology* 46, 67–75.
- 1106 Allmendinger, R.W., Cardozo, N., Fisher, D., 2012. *Structural Geology Algorithms: Vectors
1107 and Tensors in Structural Geology*. Cambridge University Press.
- 1108 Alonso-Zarza, A.M., Calvo, J.P., 2000. Palustrine sedimentation in an episodically subsiding
1109 basin: the Miocene of the northern Teruel graben (Spain). *Palaeogeography,
1110 Palaeoclimatology, Palaeoecology* 160, 1–21.
- 1111 Alonso-Zarza, A.M., Meléndez, A., Martín-García, R., Herrero, M.J., Martín-Pérez, A., 2012.
1112 Discriminating between tectonism and climate signatures in palustrine deposits: 2
1113 lessons from the Miocene of the Teruel graben, NE Spain. *Earth-Science Reviews*
1114 113 (3), 141–160.
- 1115 Alsop, G.I., Marco, S., 2013. Seismogenic slump folds formed by gravity-driven tectonics
1116 down a negligible subaqueous slope. *Tectonophysics* 605, 48–69.
- 1117 Álvaro, M., Capote, R., Vegas, R., 1979. Un Modelo de evolución geotectónica Para la
1118 Cadena Celtibérica. *Acta Geologica Hispánica* 14, 172–177.
- 1119 Bailey, R.C., Halls, H.C., 1984. Estimate of confidence in paleomagnetic directions derived
1120 from mixed magnetization circle and direct observational data. *Journal of Geophysics*
1121 54, 174–182.
- 1122 Bleakly, D.C., Van Alstine, D.R., Packer, D.R., 1985. Core orientation 1: controlling errors
1123 minimizes risk and cost in core orientation. *Oil and Gas Journal* 83 (48), 103–109.
- 1124 Capote, R., Muñoz, J.A., Simón, J.L., Liesa, C.L., Arlegui, L.E., 2002. Alpine Tectonics I: the Al-
1125 pine System north of the Betic Cordillera. In: Gibbons, W., Moreno, T. (Eds.), *Geology
1126 of Spain*. Geological Society of London, London, pp. 367–400.
- 1127 Davenport, C.A., Ringrose, P.S., 1987. Deformation of Scottish Quaternary Sediment
1128 Sequences by Strong Earthquake Motions. In: Jones, M.E., Preston, R.M.F. (Eds.),
1129 *Deformation of Sediments and Sedimentary Rocks*. The Geological Society, London,
1130 Special Publication 29, pp. 299–314.
- 1131 De Wet, C., Yocum, D.A., Mora, C., 1998. Carbonate lakes in closed basins: sensitive
1132 indicators of climate and tectonics: an example from the Gettysburg Basin (Triassic),
1133 Pennsylvania, USA. Role of Eustasy, climate and tectonism in continental rocks. *SEPM
1134 Special Publication* 59, 191–209.
- 1135 Deenen, M.H.L., Langereis, C.G., van Hinsbergen, D.J.J., Biggin, A.J., 2011. Geomagnetic
1136 secular variation and the statistics of palaeomagnetic directions. *Geophysical Journal
1137 International* 186 (2), 509–520.
- 1138 Dzylinski, S., Walton, E.K., 1965. Sedimentary Features of Flysch and Greywackes. *Develop-
1139 ments in Sedimentology* 7. Elsevier, Amsterdam.
- 1140 Eissmann, L., 1994. Grundzüge der Quartärgeologie Mitteldeutschlands (Sachsen,
1141 Sachsen-Anhalt, Südburgenland, Thüringen). *Altenburger Naturwissenschaftliche
1142 Forschung* 7, 55–135.
- 1143 El Taki, H., Pratt, B.R., 2012. Syndepositional tectonic activity in an epicontinental basin re-
1144 vealed by deformation of subaqueous carbonate laminites and evaporites: seismites
1145 in Red River strata (upper Ordovician) of southern Saskatchewan, Canada. *Bulletin
1146 of Canadian Petroleum Geology* 60 (1), 37–58.
- 1147 Ezquerro, L., Luzón, M.A., Liesa, C.L., Simón, J.L., 2012a. Evolución Megasecuenal del
1148 Relleno Mio-Plioceno del Sector Norte de la Cuenca de Teruel: Interacciones Entre
1149 tectónica y sedimentación. In: Fernández, L.P., Fernández, A., Cuesta, A.,
1150 Bahamonde, J.R. (Eds.), *GeoTemas 13. Resúmenes Extendidos Del VIII Congreso
1151 Geológico de España*, Oviedo, pp. 171–174.
- 1152 Ezquerro, L., Lafuente, P., Pesquero, M.D., Alcalá, L., Arlegui, L.E., Liesa, C.L., Luque, L.,
1153 Rodríguez-Pascua, M.A., Simón, J.L., 2012b. Una cubeta endorreica residual
1154 plio-pleistocena en la zona de relevo entre las fallas de Concud y Teruel:
1155 implicaciones paleogeográficas. *Revista de la Sociedad Geológica de España* 25,
1156 157–175.
- 1157 Ezquerro, L., Luzón, A., Navarro, M., Liesa, C.L., Simón, J.L., 2014a. Climatic vs. tectonic sig-
1158 nal in the Neogene extensional Teruel basin (NE Spain), based on stable isotope
1159 ($\delta^{18}O$) and megasequential evolution. *Terranova* 26 (5), 337–346.
- 1160 Ezquerro, L., Liesa, C.L., Simón, J.L., Arlegui, L.E., Luzón, A., Lafuente, P., 2014b. Correlation
1161 of sedimentary units from grain-size and mineralogical analyses as a tool for
1162 constraining trench interpretation in paleoseismology. *International Journal of
1163 Earth Sciences* 103 (8), 2327–2333.
- Ezquerro, L., Moretti, M., Liesa, C.L., Luzón, A., Simón, J.L., 2015. Seismites from a well core
1164 of palustrine deposits as a tool for reconstructing the palaeoseismic history of a fault.
1165 *Tectonophysics* 655, 191–205.
- 1166 Field, M.E., Gardner, V., Jennings, A.E., Edwards, B.D., 1982. Earthquake-induced sediment
1167 failures on a 0.25° slope, Klamath River delta, California. *Geology* 10, 542–546.
- 1168 Fisher, R.A., 1953. Dispersion on a sphere. *Proceedings of the Royal Astronomical Society*
1169 217, 295–305.
- 1170 Fuller, M., 1969. Magnetic orientation of borehole cores. *Geophysics* 34, 772–774.
- 1171 Garcés, M., Krijgsman, W., Van Dam, J., Calvo, J.P., Alcalá, L., Alonso-Zarza, A.M., 1999.
1172 Late Miocene alluvial sediments from the Teruel area: magnetostratigraphy,
1173 magnetic susceptibility, and facies organization. *Acta Geologica Hispánica* 32,
1174 171–184.
- 1175 García-Tortosa, F.J., Alfaro, P., Gibert, L., Scott, G., 2011. Seismically induced slump on an
1176 extremely gentle slope (<1 degrees) of the Pleistocene Tecopa paleolake (California).
1177 *Geology* 39 (11), 1055–1058.
- 1178 Gibert, L., Alfaro, P., García-Tortosa, F.J., Scott, G., 2011. Superposed deformed beds
1179 produced by single earthquakes (Tecopa Basin, California): insights into
1180 paleoseismology. *Sedimentary Geology* 235 (3–4), 148–159.
- 1181 Godoy, A., Ramírez, J.I., Olivé, A., Moissenet, E., Aznar, J.M., Aragónés, E., Aguilar, M.J.,
1182 Ramírez del Pozo, J., Leal, M.C., Jerez-Mir, L., Adrover, R., Goy, A., Comas, M.J., Alberdi,
1183 M.T., Giner, J., Gutiérrez-Elorza, M., Portero, J.M., Gabaldón, V., 1983a. Hoja geológica
1184 núm. 567 (Teruel). Mapa Geológico de España E: 1:50.000. IGME, Madrid.
- 1185 Godoy, A., Olivé, A., Moissenet, E., 1983b. Hoja geológica núm. 542 (Alfambra). Mapa
1186 Geológico de España E: 1:50.000. IGME, Madrid.
- 1187 Guiraud, M., Plaziat, J.-C., 1993. Seismites in the fluvialite Bima sandstones: identification
1188 of paleoseisms and discussion of their magnitudes in a cretaceous synsedimentary
1189 strike-slip basin (upper Benue, Nigeria). *Tectonophysics* 225, 493–522.
- 1190 Gutiérrez, F., Gutiérrez, M., Gracia, F.J., McCalpin, J.P., Lucha, P., Guerrero, J., 2008. Plio-
1191 quaternary extensional seismotectonics and drainage network development in the cen-
1192 tral sector of the Iberian range (NE Spain). *Geomorphology* 102, 21–42.
- 1193 Hailwood, E.A., Ding, F., 1995. Palaeomagnetic Reorientation of Cores and the Magnetic
1194 Fabric of Hydrocarbon Reservoir Sands. In: Turner, P., Turner, A. (Eds.),
1195 *Palaeomagnetic Applications in Hydrocarbon, Exploration and Production*. Geological
1196 Society Special Publication 98, pp. 245–258.
- 1197 Hamilton, W.D., Van Alstine, D.R., Butterworth, J.E., Raham, G., 1995. Paleomagnetic Ori-
1198 entation of Fractures in Jean Marie Member Cores from NE British Columbia/NW
1199 Alberta. *The Petroleum Society of CIM*, pp. 56–95.
- 1200 Jackson, A., Jonkers, A.R.T., Walker, M.R., 2000. Four centuries of geomagnetic secular va-
1201 riation from historical records. *Philosophical Transactions of the Royal Society of
1202 London* 358, 957–990.
- 1203 Kirschvink, J.L., 1980. The least-squares line and plane and the analysis of paleomagnetic
1204 data. *Geophysical Journal of the Royal Astronomical Society* 62, 699–718.
- 1205 Krijgsman, W., 1996. Miocene magnetostratigraphy and cyclostratigraphy in the Mediter-
1206 ranean: extension of the astronomical polarity time scale. *Geologica Ultraiectina* 141,
1207 1–207.
- 1208 Krijgsman, W., Garcés, M., Langereis, C.G., Daams, R., van Dam, J., van der Meulen, A.J.,
1209 Agustí, J., Cabrera, L., 1996. A new chronology for the middle to late Miocene
1210 continental record in Spain. *Earth and Planetary Science Letters* 142, 367–380.
- 1211 Lafuente, P., 2011. *Tectónica Activa Y Paleosismicidad de la Falla de Concud (Cordillera
1212 Ibérica Central)* PhD Thesis Universidad de Zaragoza, Zaragoza.
- 1213 Lafuente, P., Arlegui, L.E., Liesa, C.L., Simón, J.L., 2011a. Paleoseismological analysis of an
1214 intraplate extensional structure: the Concud fault (Iberian chain, Spain). *International
1215 Journal of Earth Sciences* 100, 1713–1732.
- 1216 Lafuente, P., Arlegui, L.E., Casado, I., Ezquerro, L., Liesa, C.L., Pueyo, Ó., Simón, J.L., 2011b.
1217 Geometría y cinemática de la zona de relevo entre las fallas neógeno-cuaternarias
1218 de Concud y Teruel (cordillera Ibérica). *Revista de la Sociedad Geológica de España*
1219 24, 117–132.
- 1220 Lafuente, P., Arlegui, L.E., Liesa, C.L., Pueyo, Ó., Simón, J.L., 2014. Spatial and temporal va-
1221 riation of paleoseismic activity at an intraplate, historically quiescent structure: the
1222 Concud fault (Iberian chain, Spain). *Tectonophysics*. <http://dx.doi.org/10.1016/j.tecto.2014.06.012>.
- 1223 Liesa, C.L., Rodríguez-López, J.P., Ezquerro, L., Alfaro, P., Rodríguez-Pascua, M.A., Lafuente,
1224 P., Arlegui, L., Simón, J.L., 2016. Facies control on seismites in an alluvial-aeolian sys-
1225 tem: the Pliocene dunefield of the Teruel half-graben basin (eastern Spain). *Sedimen-
1226 tary Geology*. <http://dx.doi.org/10.1016/j.sedgeo.2016.05.009>.
- 1227 Lowe, D.R., 1975. Water escape structures in coarse-grained sediments. *Sedimentology*
1228 22, 157–204.
- 1229 Lowrie, W., 1990. Identification of ferromagnetic minerals in a rock by coercivity and
1230 unblocking temperature properties. *Geophysical Research Letters* 135, 159–162.
- 1231 Luzón, A., González, A., Muñoz, A., Sánchez-Valverde, B., 2002. Upper Oligocene–lower
1232 Miocene shallowing-upward lacustrine sequences controlled by periodic and non-
1233 periodic processes (Ebro Basin, northeastern Spain). *Journal of Paleolimnology* 28,
1234 441–456.
- 1235 Mastrogiacomo, G., Moretti, M., Owen, G., Spalluto, L., 2012. Tectonic triggering of slump
1236 sheets in the upper cretaceous carbonate succession of the Porto Selvaggio area
1237 (Salento peninsula, southern Italy): synsedimentary tectonics in the Apulian carbon-
1238 ate platform. *Sedimentary Geology* 269–270, 15–27.
- 1239 Mein, P., 1975. Résultats Du Groupe de Travail Des Vertebres. Report on Activity of the
1240 R.C.M.N.S. Working Groups, Bratislava, pp. 77–81.
- 1241 Mein, P., Moissenet, E., Adrover, R., 1983. L'extension et l'âge des formations continentales
1242 pliocenes du fossé de Teruel. *Comptes Rendus de l'Académie des Sciences de Paris*
1243 296, 1603–1610.
- 1244 Mein, P., Moissenet, E., Adrover, R., 1990. Biostratigraphie du Neogene superieur de
1245 Teruel. *Paleontología i Evolució* 23, 121–139.
- 1246 Migowski, C., Agnon, A., Bookman, R., Negendank, J.F.W., Stein, M., 2004. Recurrence
1247 pattern of Holocene earthquakes along the Dead Sea transform revealed by varve-
1248 1249

- 1250 counting and radiocarbon dating of lacustrine sediments. *Earth and Planetary Science*
1251 *Letters* 222, 301–314.
- 1252 Moissenet, E., 1980. Relief et déformations récentes trois transversales dans les fossés in-
1253 ternes des chaînes Ibériques orientales. *Revue de Géographie des Pyrénées Sud-Ouest*
1254 51, 315–344.
- 1255 Moissenet, E., 1982. Le Villafranchien de la région de Teruel (Espagne). *Stratigraphie Dé-*
1256 *formations Milieux*. Colloque "Le Villafranchien méditerranéen", Lille, pp. 229–253.
- 1257 Moissenet, E., 1983. Aspectos de la Neotectónica en la Fosa de Teruel. In: Comba, J.A. (Ed.),
1258 *Geología de España Libro Jubilar J.M. Ríos vol. 2*. IGME, Madrid, pp. 427–446.
- 1259 Montenat, C., Barrier, P., d'Estevou, P.O., Hibsich, C., 2007. Seismites: an attempt at critical
1260 analysis and classification. *Sedimentary Geology* 196, 5–30.
- 1261 Moretti, M., 2000. Soft-sediment deformation structures interpreted as seismites in
1262 middle-late Pleistocene aeolian deposits (Apulian foreland, southern Italy). *Sedimen-*
1263 *tary Geology* 135, 167–179.
- 1264 Moretti, M., Ronchi, A., 2011. Liquefaction features interpreted as seismites in the Pleisto-
1265 cene fluvio-lacustrine deposits of the Neuquén Basin (northern Patagonia). *Sedimen-*
1266 *tary Geology* 235, 200–209.
- 1267 Moretti, M., Sabato, L., 2007. Recognition of trigger mechanisms for soft-sediment deforma-
1268 tion in the Pleistocene lacustrine deposits of the Sant'Arcangelo Basin (southern
1269 Italy): seismic shock vs. overloading. *Sedimentary Geology* 196, 31–45.
- 1270 Moretti, M., Van Loon, A.J., 2014. Restrictions to the application of 'diagnostic' criteria for
1271 recognizing ancient seismites. *Journal of Palaeogeography* 3 (2), 162–173.
- 1272 Moretti, M., Alfaro, P., Caselles, O., Canas, J.A., 1999. Modelling seismites with a digital
1273 shaking table. *Tectonophysics* 304, 369–383.
- 1274 Moretti, M., Soria, J.M., Alfaro, P., Walsh, N., 2001. Asymmetrical soft-sediment deforma-
1275 tion structures triggered by rapid sedimentation in turbiditic deposits (late Miocene,
1276 Guadix Basin, southern Spain). *Facies* 44, 283–294.
- 1277 Obermeier, S.F., 1996. Use of liquefaction-induced features for paleoseismic analysis - an
1278 overview of how seismic liquefaction features can be distinguished from other fea-
1279 tures and how their regional distribution and properties of source sediment can be
1280 used to infer the location and strength of Holocene paleo-earthquakes. *Engineering*
1281 *Geology* 44 (1–4), 1–76.
- 1282 Obermeier, S.F., Gohn, G.S., Weems, R.E., Gelinas, R.L., Rubin, M., 1985. Geologic evidence
1283 for recurrent moderate to large earthquakes near Charleston, South Carolina. *Science*
1284 277, 408–410.
- 1285 Ogg, J.G., 2012. Chapter 5: Geomagnetic Polarity Time Scale. In: Gradstein, F.M., Ogg, J.G.,
1286 Schmitz, M.D., Ogg, G.M. (Eds.), *The Geologic Time Scale*. Elsevier, Amsterdam.
- 1287 Opdyke, N., Channell, J.E., 1996. *Magnetic Stratigraphy* 64. Academic Press, San Diego.
- 1288 Opdyke, N., Mein, P., Lindsay, E., Pérez-González, A., Moissenet, E., Norton, V.L., 1997.
1289 *Palaeogeography, Palaeoclimatology, Palaeoecology* 133, 129–148.
- 1290 Osete, M.L., Palencia, A., 2006. Polos paleomagnéticos de los últimos 300 millones de años.
1291 *Física de la Tierra* 18, 157–181.
- 1292 Owen, G., 1987. Deformation Processes in Unconsolidated Sands. In: Jones, M.E., Preston,
1293 R.M.F. (Eds.), *Geological Society Spec. Publ.* 29, pp. 11–24.
- 1294 Owen, G., Moretti, M., 2008. Determining the origin of soft-sediment deformation struc-
1295 tures: a case study from upper carboniferous delta deposits in south-west wales,
1296 UK. *Terra Nova* 20, 237–245.
- 1297 Owen, G., Moretti, M., 2011. Identifying triggers for liquefaction-induced soft-sediment
1298 deformation in sands. *Sedimentary Geology* 235, 141–147.
- 1299 Owen, G., Moretti, M., Alfaro, P., 2011. Recognising triggers for soft-sediment deforma-
1300 tion: current understanding and future directions. *Sedimentary Geology* 235,
1301 133–140.
- 1302 Peña, J.L., Gutiérrez, M., Ibáñez, M.J., Lozano, M.V., Rodríguez, J., Sánchez, M., Simón, J.L.,
1303 Soriano, M.A., Yetano, L.M., 1984. Geomorfología de la Provincia de Teruel. Instituto
1304 de Estudios Turolenses, Teruel.
- 1305 Posamentier, H.W., Allen, G.P., 1999. *Siliciclastic Sequence Stratigraphy: Concepts and Ap-*
1306 *plications*. SEPM Concepts in Sedimentology and Paleontology 7, Tulsa.
- 1307 Pueyo, E., Garcés, M., Mauritsch, H.J., Lewis, C., Scholger, R., Sancho, C., Molina, R., Schnepf,
1308 E., Larrasoana, J.C., Parés, J.M., Pucoví, A., Muñoz, A., Valero, B., Millán, H., Laplana, C.,
1309 Oliva, B., González, P., 2006. Sampling, Transportation and Magnetic-Free Consolidation
1310 of extremely Soft Sediments for Paleomagnetic Purposes: a Successful Recipe?
1311 In: Calvo, M., Garcés, M., Gomes, C., Larrasoana, J., Pueyo, E., Villalain, J. (Eds.),
1312 *Paleomagnetismo en la Península Ibérica: MAGIBER I*, Burgos, pp. 119–126.
- 1313 Ramón, M.J., 2013. Flexural unfolding of complex geometries in fold and thrust belts
1314 using paleomagnetic vectors. Unpublished PhD University of Zaragoza, 228 pp.
1315 <http://zaguan.unizar.es/record/11750>
- 1316 Ramón, M.J., Pueyo, E.L., 2012. Automatic Calculation of Demagnetization Intervals; a New
1317 Approach Based on the Virtual Directions Method and Comparison with the Linearity
1318 Spectrum Analysis. In: Fernández, L.P., Fernández, A., Cuesta, A., Bahamonde, J.R.
1319 (Eds.), *GeoTemas 13. Resúmenes Extendidos Del VIII Congreso Geológico de España*,
1320 Oviedo, pp. 1180–1183.
- 1321 Rodríguez-López, J.P., Meléndez, N., Soria, A.R., Liesa, C.L., Van Loon, A.J., 2007. Lateral vari-
1322 ability of ancient seismites related to differences in sedimentary facies (the synrift
1323 Escucha formation, mid-cretaceous, eastern Spain). *Sedimentary Geology* 201,
1324 461–484.
- 1325 Rodríguez-Pascua, M.A., Calvo, J.P., De Vicente, G., Gómez-Gras, D., 2000. Soft-sediment
1326 deformation structures interpreted as seismites in lacustrine sediments of the
1327 Prebetic zone, SE Spain, and their potential use as indicators of earthquake magni-
1328 tudes during the late Miocene. *Sedimentary Geology* 135, 117–135.
- Rubio, J.C., Simón, J.L., 2007. Tectonic subsidence vs. erosional lowering in a controversial
intra-montane depression: the Jiloca basin (Iberian chain, Spain). *Geological Magazine*
144, 1–15.
- Shibuya, H., Merril, D., Hsu, V., Leg, 124, Shipboard Scientific Party, 1991. Paleogene
Counter-clockwise Rotation of the Celebes Sea—Orientation of ODP Cores Utilizing
the Secondary Magnetization. In: Silver, E.A., Rangin, C., von Breymann, M.T. (Eds.),
Proceedings of the Ocean Drilling Program. Scientific Results 124, pp. 519–522.
- Simón, J.L., 1982. *Compresión Y distensión Alpinas en la Cadena Ibérica Oriental* PhD.
Thesis Universidad de Zaragoza. Publ. Instituto de Estudios Turolenses, Teruel.
- Simón, J.L., 1983. *Tectónica Y neotectónica Del Sistema de Fosas de Teruel* 69 pp. 21–97
Teruel.
- Simón, J.L., Arlegui, L.E., Lafuente, P., Liesa, C.L., 2012. Active extensional faults in the
central-eastern Iberian chain, Spain. *Journal of Iberian Geology* 38, 127–144.
- Simón, J.L., Arlegui, L.E., Ezquerro, L., Lafuente, P., Liesa, C.L., 2014. Aproximación a la
peligrosidad sísmica en la ciudad de Teruel asociada a la falla de Conclud (NE España).
Geogaceta 5, 7–10.
- Simón, J.L., Arlegui, L.E., Ezquerro, L., Lafuente, P., Liesa, C.L., Luzón, A., 2015. Enhanced
paleoseismic succession at the Conclud fault (Iberian chain, Spain): new insights for
seismic hazard assessment. *Natural Hazards*. <http://dx.doi.org/10.1007/s11069-015-2054-6>.
- Simón, J.L., Arlegui, L.E., Ezquerro, L., Lafuente, P., Liesa, C.L., Luzón, A., 2016. Structure and
paleoseismology of the Teruel fault: dynamic interaction and strain partitioning with
the Conclud fault (eastern Iberian chain, Spain). *Journal of Structural Geology* (in
press).
- Sims, J.D., 1975. Determining earthquake recurrence intervals from deformational struc-
tures in young lacustrine sediments. *Tectonophysics* 29, 141–152.
- Sinusúa, C., Pueyo, E.L., Azanza, B., Pucoví, A., 2004. Datación magnetoestratigráfica del
yacimiento paleontológico de Puebla de Valverde (Teruel). *GeoTemas* 6 (4), 339–342.
- Soria, A.R., Muñoz, A., Liesa, C.L., Luzón, A., Meléndez, A., Meléndez, M.N., 2013. Climate-
driven cyclicity in an early cretaceous synrift lacustrine series (Aguilón sub-basin,
NE Spain). *Terra Nova* 24, 407–416.
- Spalluto, L., Moretti, M., Festa, V., Tropeano, M., 2007. Seismically-induced slumps in
lower-Maastrichtian peritidal carbonates of the Apulian platform (southern Italy).
Sedimentary Geology 196, 81–98.
- Stárková, M., Martinek, K., Mikuláš, R., Rosenau, N., 2015. Types of soft-sediment deforma-
tion structures in a lacustrine Ploužnice member (Stephanian, Gzhelian, Pennsylvanian,
bohemian massif), and possible trigger mechanism. *International Journal of Earth Sciences*
104, 1277–1298.
- Stokking, L.B., Musgrave, R.J., Bontempo, D., Autio, W., 1993. Handbook for shipboard Pa-
leomagnetists. ODP tech. Note, 18: College Station, TX (ocean drilling program).
http://www-odp.tamu.edu/publications/notes/tn18/f_pal.htm.
- Thibaut, J., Etchecopar, A., Pozzi, J.P., Barthès, V., Pocachard, J., 1999. Comparison of magnetic
and gamma ray logging for correlations in chronology and lithology: example from
the Aquitanian Basin (France). *Geophysical Journal International* 137, 839–846.
- Tuttle, M.P., Schweig, E.S., Sims, J.D., Lafferty, R.H., Wolf, L.W., Haynes, M.L., 2002. The
earthquake potential of the New Madrid seismic zone. *Bulletin of the Seismological Society of America* 92,
2080–2089.
- Van Alstine, D.R., Butterworth, J.E., 1993. Paleomagnetic orientation of fractures and bed-
ding in Rotliegend and Zechstein cores from the southern Permian Basin, North Sea.
AAPG Bulletin 77, 1672.
- Van Alstine, D.R., Butterworth, J.E., Willemse, E.J.M., Van de Graaff, W.J.E., 1991. Paleomag-
netic core-orientation for characterizing reservoir anisotropy: case histories from
fractured reservoirs in Abu Dhabi and Venezuela. *AAPG Bulletin* 75, 687.
- van Dam, J.A., 2006. Geographic and temporal patterns in the late Neogene (12–3 Ma)
aridification of Europe: the use of small mammals as paleoprecipitation proxies.
Palaeogeography, Palaeoclimatology, Palaeoecology 238, 190–218.
- van Dam, J.A., Alcalá, L., Alonso-Zarza, A.M., Calvo, J.P., Garcés, M., Krijgsman, W., 2001.
High-resolution late Miocene mammal biochronology and paleoecology of the
Teruel–Alfambra region (NE Spain). *Journal of Vertebrate Paleontology* 21, 367–385.
- Van der Voo, R., Watts, D.R., 1978. Paleomagnetic results from igneous and sedimentary
rocks from the Michigan Basin borehole. *Journal of Geophysical Research* 83,
5844–5848.
- Van Loon, A.J., 2009. Soft-sediment deformation structures in siliciclastic sediments: an
overview. *Geologos* 15, 3–55.
- Van Loon, A.J., Brodzikowski, K., Zielinski, 1995. Shock-induced resuspension deposits
from a Pleistocene glacial lake (Kleszczów graben, Central Poland). *Journal of Sediment-
ary Research* A65 (2), 417–422.
- Vandamme, D., 1994. A new method to determine paleosecular variation. *Physics of the Earth and Planetary Interiors* 85,
131–142.
- Weerd, A., 1976. *Rodent Faunas of the Mio-Pliocene Continental Sediments of the Teruel Alfambra Region, Spain* PhD. Thesis Utrecht Micropaleontol. Bulletin, Special Publication 2, Utrecht.
- Zhang, F.Q., Song, J.S., Shen, Z.Y., Chen, H.L., Dong, C.W., Pang, Y.M., Shu, P., 2007. A study on
fracture orientation and characteristic of remnant magnetization of deep-burial
volcanic rocks, north of the Songliao Basin. *Chinese Journal of Geophysics* 50 (4),
1011–1017.